

Scattering of flexural–gravity waves at the boundaries between three floating sheets with applications

By T. D. WILLIAMS AND V. A. SQUIRE†

Department of Mathematics and Statistics, University of Otago, PO Box 56, Dunedin, New Zealand

(Received 21 March 2006 and in revised form 30 May 2006)

A theoretical model is reported that describes wave propagation between three floating Euler–Bernoulli thin elastic sheets extending, respectively, from $-\infty$ to 0, from 0 to l , and from l to ∞ , with properties, e.g. thickness, that can be specified independently. The sheets are assumed either to be welded together or to have free edges separating them. Two methods of solution are employed – the Wiener–Hopf technique and residue calculus, which allows the theoretical development to be verified at various points along the way. The model generalizes the considerable body of published work concerned with wave propagation into and out of floating ice sheets, and across features contained therein such as cracks, open or refrozen leads and embedded icebergs. It can also be applied to breakwaters, very large floating structures and vessels in a seaway. After validation, results are presented showing (*a*) the details of how the reflection coefficient depends on the geometry of the configuration being modelled; and (*b*) how a wave energy spectrum evolves as it propagates in a marginal ice zone composed of a large number of identical (coherent) or randomly specified (incoherent) sea-ice plates, as commonly observed in the polar or subpolar oceans.

1. Introduction

Ocean waves propagating across the Arctic sea-ice canopy will encounter many irregularities during their passage. First, as they enter the ice cover – typically from the North Atlantic Ocean, they will experience an impedance change as they depart the open water. This was modelled initially by Fox & Squire (1990, 1994), building on the incomplete work of Evans & Davies (1968). It results in altered dispersion, as the waves are now influenced by the flexural properties of the sea-ice under which they travel, as well as by gravity; accordingly, the prefix ‘flexural–gravity’ is commonly applied to describe such waves. Once inside the ice cover, the waves’ course is affected by leads – either open or refrozen, pressure ridges, ice thickness variations, and physical and mechanical changes in the properties of the sea-ice. Each of these features causes some reflection to occur in a manner that is known to favour the passage of long period waves over short periods, so, as explained in Squire *et al.* (1995), the integrated effect of coming upon many heterogeneities over large distances is a gradual evolution of the wave spectrum towards longer period energy and the removal of short period waves. Squire *et al.* report several examples of this and also include a description of what was known at the time about wave propagation in the

† Author to whom correspondence should be addressed: vernon.squire@otago.ac.nz.

marginal ice zone (MIZ): typically a 10–100 km wide band of broken-up pack ice floes and cakes that skirts the more continuous interior sea-ice and which is affected significantly by open ocean processes. MIZs are present in both polar regions and have an important impact on regional climate because their constituent sea-ice alters the way the atmosphere couples to the ocean. Taken in the context of global warming, this is of immediate topical significance, as temporal adjustments in pack ice serve as a proxy of climate change (see, e.g. Rothrock, Yu & Maykut 1999; Wadhams & Davis 2000; Comiso 2002).

Squire *et al.* includes a discussion of some theoretical modelling, but considerable progress has been made post 1995 towards constructing physically more realistic ice sheets that can incorporate the inhomogeneities described above. Since that time, a series of papers have appeared to determine the scattering kernels associated with various irregularities in an ice sheet, in the majority of cases using an Euler–Bernoulli plate to represent the sea-ice. Numerical methods as well as mathematical ones such as the Wiener–Hopf technique and residue calculus have been used. Solutions include wave entry at the ice sheet margin or across an abrupt change of thickness (Evans & Davies 1968; Gol'dshtein & Marchenko 1989; Barrett & Squire 1996; Balmforth & Craster 1999; Chakrabarti 2000; Chung & Fox 2002*a*; Sahoo, Yip & Chwang 2001; Tkacheva 2001; Chung & Fox 2002*b*; Linton & Chung 2004) and wave propagation across single or multiple cracks (Marchenko 1997; Chou 1998; Squire & Dixon 2000, 2001*a*; Williams & Squire 2002; Evans & Porter 2003; Manam, Bhattacharjee & Sahoo 2005); an open or refrozen lead (Williams & Squire 2004*a*; Chung & Linton 2005); a localized change of thickness resulting from, for example, a trapped iceberg (Squire & Dixon 2001*b*; Williams & Squire 2004*a*); and a pressure ridge (Williams & Squire 2004*a*; Porter & Porter 2004).

A similar problem is the scattering by a floating strip. Meylan (1993) and Meylan & Squire (1994) used the solution of an integral equation derived from Green's theorem by using Gaussian quadrature. Hermans (2003) took a similar approach, but solved the integral equation by using a Galerkin expansion. Tkacheva (2002, 2004) also solved the problem by deriving a pair of coupled Wiener–Hopf equations directly in Fourier transform space. As in the present paper, this produces an efficient solution method as only the evanescent waves that have not decayed by the time they cross the strip need be considered. In parallel, modelling work focused on the MIZ has also become more sophisticated by embedding the flexible floating raft in a Boltzmann equation formulation (see, e.g. Meylan & Squire 1996; Meylan, Squire & Fox 1997; Meylan & Masson 2006; Peter, Meylan & Linton 2006).

The current paper extends these solutions further by introducing appreciably greater generality: we allow the ice properties and, in particular, the ice thickness to be specified entirely independently in each of three regions extending from $-\infty$ to 0, from 0 to l , and from l to ∞ . By doing this, gravity wave propagation across irregularities such as open or refrozen leads in polar sea-ice, between adjacent ice floes in pack ice, from open sea into shore fast ice or vice versa, across an iceberg embedded in a sea-ice sheet, and into an ice shelf, can each be studied because the theoretical development is robust enough for any of the three sheet thicknesses to be set to any value, including zero. In addition, Appendix A provides a proof that the velocity potential may always be represented by an eigenfunction expansion – a result that will be of interest to floating body researchers generally.

While the foremost application of the work reported in this paper is to polar marine geophysics, its generality also allows the model to be useful in marine engineering. Specifically, it is of value to the study of the behaviour of floating breakwaters, very

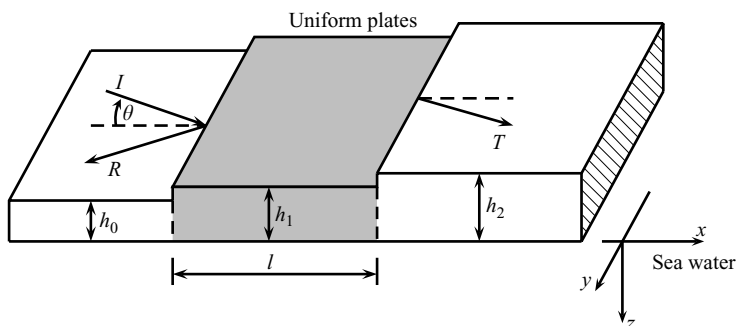


FIGURE 1. Three uniform Euler–Bernoulli thin elastic plates, floating on the fluid foundation $-\infty < x, y < \infty, 0 < z < H$ (the coordinate axes are shown displaced to the right to avoid clutter). Submergence has been neglected, so the underside of each plate lies in the $z = 0$ plane. A plane flexural–gravity wave arrives from the left ($-\infty < x < 0$) at an angle θ to normal incidence, travels through the central strip ($0 < x < l$), and then propagates into the zone on the right ($l < x < \infty$). The thickness of any of the plates may be set to zero to produce a region of open water.

large floating structures (VLFSs) and, recognizing that the model is not fully three-dimensional, the description of the response of floating vessels in a seaway. Because of this, the theoretical narrative will be framed hereinafter so as to avoid focusing prematurely on any of the specific problems mentioned, but the examples given in §5 to demonstrate the versatility of the approach will be redirected towards polar marine geophysics.

2. Equations and boundary conditions

Figure 1 illustrates the situation that we are modelling: three floating uniform flexible sheets of thickness h_0, h_1 and h_2 , as shown, either welded together or free to move independently. Each sheet is modelled as a separate Euler–Bernoulli thin elastic plate. A plane flexural–gravity wave with unit amplitude and radial frequency ω arrives at the central plate from the left-hand region and is partially reflected and partially transmitted through the central strip of width l into the right-hand region. Throughout the paper, the subscripts of $j = 0, 1$ and 2 will be used to denote quantities associated with the left-hand, central and right-hand regions, respectively.

The amplitudes of the reflected and transmitted waves, denoted by R and T , respectively, will be called the reflection and transmission coefficients. It is the determination of these quantities that is the main purpose of our solution.

Assuming that the sea water beneath the three plates is inviscid and of constant density and that the fluid flow is irrotational, then there exists a potential function $\Phi(x, y, z, t)$ such that the velocity of a fluid particle is given by $\nabla\Phi$. Because the incident wave forcing is periodic in time t , and since the geometry of the problem is shift-invariant in the y -direction, we may conclude that Φ has the following form:

$$\Phi(x, y, z, t) = \text{Re}[\phi(x, z) \exp(i(\alpha_y y - \omega t))]. \quad (2.1)$$

This reduces the dimension of the problem from four to two. The wavenumber α_y is related to the incoming wave's angle of incidence θ .

For each plate, let us now define the flexural rigidity, D_j , the mass per unit area, m_j , and the characteristic length and time, L_j and τ_j , respectively, as follows:

$$D_j = \frac{E_j h_j^3}{12(1 - \nu_j)^2}, \quad m_j = \rho_j h_j, \quad L_j = \sqrt[4]{\frac{D_j}{\rho g}}, \quad \tau_j = \sqrt{\frac{L_j}{g}}.$$

E_j , ν_j and ρ_j are, respectively, the Young's modulus, Poisson's ratio and density of the plate in the j th region, while ρ is the water density and g is the acceleration due to gravity.

We now denote by the index m the region with the largest flexural rigidity, and define the natural length $L = (D_m/\rho\omega^2)^{1/5}$ that we will use to non-dimensionalize lengths. If we also scale time t by a factor of τ_m , then we have the following quantities:

$$(\bar{x}, \bar{y}, \bar{z}) = (x, y, z)/L, \quad \bar{t} = t/\tau_m, \quad \bar{\phi}(\bar{x}, \bar{z}) = \frac{\tau_m}{L^2} \phi(x, z), \quad \bar{\alpha}_y = \alpha_y L.$$

The other two significant lengths, l and H , are also scaled by L , so that $\bar{l} = l/L$ and $\bar{H} = H/L$. Further quantities that we will refer to are

$$\bar{D}_j = D_j/D_m, \quad \bar{m}_j = m_j/m_m, \quad \lambda = \frac{g}{L\omega^2} - i\varepsilon, \quad \mu = \frac{m_m}{\rho L},$$

where ε is an infinitesimal quantity introduced to force the reflected and transmitted waves to decay exponentially as they travel away from the central strip. The limit as it becomes zero will be taken once the solution has been completed; this procedure is justified in Appendix A.

Dropping the overbars to avoid clutter, $\phi(x, z)$ must satisfy the following system of equations

$$(\nabla^2 - \alpha_y^2)\phi(x, z) = 0, \quad (2.2a)$$

$$\mathcal{L}(x, \partial_x)\phi_z(x, 0) + \phi(x, 0) = 0, \quad (2.2b)$$

$$\phi_x(x^+, z) - \phi_x(x^-, z) = \phi(x^+, z) - \phi(x^-, z) = 0, \quad (2.2c)$$

$$\phi_z(x, H) = 0, \quad (2.2d)$$

where

$$\mathcal{L}(x, \partial_x) = D(x)(\partial_x^2 - \alpha_y^2)^2 + \lambda - m(x)\mu.$$

The function $D(x)$ is defined piecewise as

$$D(x) = \begin{cases} D_0 & \text{for } x < 0, \\ D_1 & \text{for } 0 < x < l, \\ D_2 & \text{for } x > l, \end{cases}$$

and $m(x)$ is defined analogously in terms of the m_j .

As well as applying the above equations and the inherent radiation conditions (which will be defined formally in §3.2), the full solution must also satisfy some conditions at the two edges $x_e = 0$ and $x_e = l$. If two adjacent plates are joined or frozen together at a given edge, then the following fixed-edge conditions must hold:

$$\phi_z(x_e^+, 0) = \phi_z(x_e^-, 0), \quad (2.3a)$$

$$\phi_{zx}(x_e^+, 0) = \phi_{zx}(x_e^-, 0), \quad (2.3b)$$

$$D(x_e^+)\mathcal{L}_-(\partial_x)\phi_z(x_e^+, 0) = D(x_e^+)\mathcal{L}_-(\partial_x)\phi_z(x_e^-, 0), \quad (2.3c)$$

$$D(x_e^+)\mathcal{L}_+(\partial_x)\phi_{zx}(x_e^+, 0) = D(x_e^+)\mathcal{L}_+(\partial_x)\phi_{zx}(x_e^-, 0), \quad (2.3d)$$

where

$$\mathcal{L}_{\pm}(\partial_x) = (\partial_x^2 - \alpha_y^2) \mp (1 - \nu)\alpha_y^2.$$

If, on the other hand, the two plates are free to move independently, then we must apply the free-edge conditions

$$D(x_e^{\pm})\mathcal{L}_{-}(\partial_x)\phi_z(x_e^{\pm}, 0) = 0, \quad (2.4a)$$

$$D(x_e^{\pm})\mathcal{L}_{+}(\partial_x)\phi_{zx}(x_e^{\pm}, 0) = 0. \quad (2.4b)$$

Both of these sets of conditions imply that energy is conserved at each edge, i.e. no translational or rotational work is done by any of the edges. Note that even if the free-edge conditions (2.4) are applied, (2.3c) and (2.3d) are still satisfied.

3. Solution using the Wiener–Hopf technique

The first step is to use Green’s theorem to derive a pair of coupled integral equations of Wiener–Hopf type (Noble 1958; Roos 1969). These depend on $\phi_z(x, 0)$ over the two semi-infinite intervals $x \in (-\infty, 0)$ and $x \in (l, \infty)$.

Having derived the two integral equations, we then take their Fourier transforms and solve each one individually, assuming that the solution to the other is known. This produces two infinitely long unknown vectors. The first of these contains the coefficients of the individual wave modes that travel across the central region from left to right, and the second contains the coefficients of the modes that travel from right to left. The first vector depends on the coefficients of the wave modes that still have significant amplitudes after travelling from $x = l$ to $x = 0$, while the second depends on the coefficients of those modes that are still significantly large after travelling from 0 to l .

Since most of the wave modes are evanescent, i.e. they decay exponentially with distance, the two vectors are largely independent and only a small system of linear equations remains to be solved to decouple the effects of the waves that cannot be neglected after travelling across the central section.

After obtaining the general solution to the problem, we must then apply the appropriate edge conditions – either (2.3) or (2.4). Because the same process must be followed for the residue calculus technique, the description of this procedure is left to §4.3.

3.1. Green’s function

We use a Green’s function that satisfies the following set of equations:

$$(\partial_{\xi}^2 + \partial_{\zeta}^2 - \alpha_y^2)G(x - \xi, z, \zeta) = \delta(x - \xi, z - \zeta), \quad (3.1a)$$

$$\mathcal{L}_1(\partial_{\xi})G_{\zeta}(x - \xi, z, 0) + G(x - \xi, z, 0) = 0, \quad (3.1b)$$

$$G_{\zeta}(x - \xi, z, H) = 0, \quad (3.1c)$$

where $\mathcal{L}_j(\partial_x) = D_j(\partial_x^2 - \alpha_y^2) + \lambda - m_j\mu$.

This Green’s function depends on the dispersion function for the central strip $f_1(\gamma)$, where $f_j(\gamma) = \coth(\gamma H)/\gamma - \Lambda_j(\gamma)$, $\Lambda_j(\gamma) = \mathcal{L}_j(i\alpha) = D_j\gamma^4 + \lambda - m_j\mu$ ($j = 0, 1, 2$) and $\gamma(\alpha) = (\alpha^2 + \alpha_y^2)^{1/2}$. Evans & Porter (2003) present G as an inverse Fourier transform with respect to $x - \xi$:

$$\begin{aligned} G(x - \xi, z, \zeta) &= \frac{1}{2\pi} \int_{-\infty}^{\infty} \chi(z_-, \alpha) \frac{\varphi(z_+, \alpha)}{f_1(\gamma)} e^{i\alpha(\xi - x)} d\alpha \\ &= i \sum_{\alpha \in S_1} \hat{A}_1(\alpha) e^{i\alpha|x - \xi|} \varphi(z, \alpha) \varphi(\zeta, \alpha), \end{aligned} \quad (3.2)$$

where $z_- = \min\{z, \zeta\}$, $z_+ = \max\{z, \zeta\}$, and

$$\chi(z, \alpha) = \frac{\Lambda_1(\gamma)\gamma \cosh(\gamma z) - \sinh(\gamma z)}{\gamma^2 \tanh(\gamma H)}, \quad \varphi(z, \alpha) = \frac{\cosh \gamma(z - H)}{\cosh(\gamma H)}.$$

For $j=0, 1, 2$, $S_j = \{\alpha \mid f_j(\gamma)=0 \text{ and } \text{Im}(\alpha) > 0\}$ and $\hat{A}_j(\alpha) = A_j(\alpha)\Lambda_j^2(\alpha)$, where

$$A_j(\alpha) = (df_j(\gamma)/d\alpha)^{-1} = -(\gamma^2/\alpha)/(H(\Lambda_j^2(\gamma)\gamma^2 - 1) + 5D_j\gamma^4 + \lambda - m_j\mu).$$

In the limit as ε becomes zero in the definition of λ , the roots γ of each dispersion relation $f_j(\gamma)=0$ are usually distributed throughout the complex plane as shown by Fox & Squire (1990). There is one positive real root that we label γ_j , a complex conjugate pair in the right half-plane, an infinity of pure imaginary roots in the upper half-plane, and the negatives of the previously mentioned roots. The effect of ε on the location of the roots is to produce an infinitesimal counter-clockwise rotation. In particular, each γ_j is moved slightly off the real line into the upper half-plane.

The elements of each set S_j are given by $\alpha = \sqrt{\gamma^2 - \alpha_y^2}$, taking the square root from the upper half-plane. If $\varepsilon=0$ and $\alpha_y < \gamma_j$, S_j also contains a real root, α_j , that moves into the upper half-plane as ε is increased slightly. This forces the sum in (3.2) to decay exponentially as $|x - \xi| \rightarrow \infty$. The other members of S_j are two complex roots with the same imaginary parts and an infinity of pure imaginary roots.

If $\alpha_y < \gamma_0$, then $\alpha_y = \gamma_0 \sin \theta$, where θ is the angle of incidence. If $\alpha_y \geq \gamma_0$, then no propagating waves can exist in the left hand region – in that case, waves may travel parallel to the central strip but decay exponentially with distance in the perpendicular direction (Evans & Porter 2003).

Before moving on to the next section, we point out here that in the results section we present results only for infinite depth, and consequently could have used the infinite depth Green's function. However, doing this introduces branch cuts into the dispersion relation along the lines $\pm i[\alpha_y, \infty)$, and the discrete set of zeros of the finite-depth relation were thought to be more convenient to deal with, as well as giving a more general theory. In practice, the infinite-depth results can be obtained by simply choosing a large enough value of H .

3.2. Derivation of the Wiener–Hopf integral equations

The radiation conditions alluded to above require that in the limit as $\varepsilon \rightarrow 0$, the potential corresponds to an incident wave arriving from the left and being either reflected or transmitted, i.e.

$$\phi(x, z) \sim \begin{cases} (e^{i\alpha_0 x} + R e^{-i\alpha_0 x})\varphi_0(z) & \text{as } x \rightarrow -\infty, \\ T e^{i\alpha_2 x} \varphi_2(z) & \text{as } x \rightarrow \infty, \end{cases} \quad (3.3)$$

where $\varphi_j(z) = \varphi(z, \alpha_j)$ for $j=0, 1, 2$.

For $\varepsilon > 0$, $|\phi|$ will become infinite as $x \rightarrow -\infty$ due to the $\exp(i\alpha_0 x)$ term in the incident wave potential $\phi_0(x, z) = \exp(i\alpha_0 x)\varphi_0(z)$; we will instead solve for the function $\psi(x, z) = \phi(x, z) - \phi_0(x, z)$, which decays exponentially as $|x| \rightarrow \infty$.

We begin the solution by using Green's theorem to derive a pair of coupled integral equations of the Wiener–Hopf type. Using equations (2.2) and (3.1), ψ can be written

$$\psi(x, z) = \iint_{\Omega} (\nabla_{\xi\zeta}^2 G\psi - G\nabla_{\xi\zeta}^2 \psi) d\xi d\zeta = \oint_{\partial\Omega} (\partial_n G\psi - G\partial_n \psi) ds, \quad (3.4a)$$

$$= - \int_{-\infty}^{\infty} (G_{\zeta}(x - \xi, z, 0)\psi(\xi, 0) - G(x - \xi, z, 0)\psi_z(\xi, 0)) d\xi, \quad (3.4b)$$

where Ω is the fluid region, $\{(\xi, \zeta) | -\infty < \xi < \infty \text{ and } 0 < \zeta < H\}$, $\partial\Omega$ is the positively oriented boundary of Ω , s is the arclength as we travel round $\partial\Omega$, and ∂_n is the derivative with respect to the outward normal to $\partial\Omega$. Equation (3.4b) follows from (3.4a) because the exponential decay of G and ψ as $|\xi| \rightarrow \infty$, along with the sea floor conditions (2.2d) and (3.1c), force the other line integrals to vanish. If we eliminate G and ψ from (3.4b) using (2.2b) and (3.1b), integrate by parts and simplify the resulting expression, we can write ψ entirely in terms of $\psi_z(x, 0)$ for $x < 0$ and $\phi_z(x, 0)$ for $x > l$, as follows:

$$\begin{aligned} \psi(x, 0) &= \mathbf{P}_0^T \mathcal{L}_{edge}(\partial_x) G_\zeta(x, z, 0) + \mathbf{P}_l^T \mathcal{L}_{edge}(\partial_x) G_\zeta(x-l, z, 0) \\ &+ \int_0^\infty (\mathcal{L}_1 - \mathcal{L}_0) G_\zeta(x-\xi, z, 0) \phi_{0,z}(\xi, 0) d\xi \\ &+ \int_{-\infty}^0 (\mathcal{L}_0 - \mathcal{L}_1) G_\zeta(x-\xi, z, 0) \psi_z(\xi, 0) d\xi \\ &+ \int_l^\infty (\mathcal{L}_2 - \mathcal{L}_1) G_\zeta(x-\xi, z, 0) \phi_z(\xi, 0) d\xi, \end{aligned} \quad (3.5)$$

where $\mathbf{P}_{x_e} = \mathbf{P}_{x_e}^+ - \mathbf{P}_{x_e}^-$ and

$$\mathcal{L}_{edge}(\partial_x) = - \begin{pmatrix} \mathcal{L}_+(\partial_x) \partial_x \\ \mathcal{L}_-(\partial_x) \\ \partial_x \\ 1 \end{pmatrix}, \quad \mathbf{P}_{x_e}^\pm = D(x_e^\pm) \begin{pmatrix} 1 \\ \partial_x \\ \mathcal{L}_-(\partial_x) \\ \mathcal{L}_+(\partial_x) \partial_x \end{pmatrix} \phi_z(x_e^\pm, 0).$$

We now differentiate equation (3.5) with respect to z and let $z \rightarrow 0$ to give an integral equation in $\psi_z(x, 0)$. We will solve it by splitting it into two different equations, corresponding to regions 0 and 2; these are

$$\psi_-(x) = \sum_{\alpha \in S_1} \beta_+(\alpha) e^{-i\alpha x} + \int_{-\infty}^0 (\mathcal{L}_0 - \mathcal{L}_1) g(x-\xi) \psi_-(\xi) d\xi, \quad (3.6a)$$

$$\phi_+(x) = \sum_{\alpha \in S_1} \beta_-(\alpha) e^{i\alpha(x-l)} + \int_l^\infty (\mathcal{L}_2 - \mathcal{L}_1) g(x-\xi) \phi_+(\xi) d\xi, \quad (3.6b)$$

where $\psi_-(x) = \psi_z(x, 0)$ when $x < 0$, $\phi_+(x) = \phi_z(x, 0)$ when $x > l$, and

$$g(x-\xi) = G_{z\zeta}(x-\xi, 0, 0) = \frac{1}{2\pi} \int_{-\infty}^\infty \frac{1}{f_1(\gamma)} e^{-i\alpha(x-\xi)} d\alpha = i \sum_{\alpha \in S_1} A_1(\alpha) e^{i\alpha|x-\xi|}. \quad (3.7)$$

If $\mathbf{p}(\alpha) = \mathcal{L}_{edge}(-i\alpha)$ and $F_0(\alpha) = \mathbf{p}^T(\alpha) \mathbf{P}_0 + i f_0(\gamma) \phi_0'(0) / (\alpha + \alpha_0)$, then the β_\pm coefficients are

$$\beta_+(\alpha) = i A_1(\alpha) F_0(\alpha) + c(\alpha) e^{i\alpha l}, \quad (3.8a)$$

$$\beta_-(\alpha) = i A_1(\alpha) \mathbf{p}^T(-\alpha) \mathbf{P}_l + b(\alpha) e^{i\alpha l}. \quad (3.8b)$$

The b and c coefficients in (3.8) correspond to the eigenfunction expansion of $\phi_z(x, 0)$ in the central region

$$\phi_z(x, 0) = \sum_{\alpha \in S_1} (b(\alpha) e^{i\alpha x} + c(\alpha) e^{i\alpha(l-x)}) \quad \text{for } 0 < x < l. \quad (3.9)$$

They are given by

$$b(\alpha) = i A_1(\alpha) (F_0(-\alpha) - f_0(\gamma) \Psi^-(-\alpha)), \quad (3.10a)$$

$$c(\alpha) = iA_1(\alpha)(\mathbf{p}^T(\alpha)\mathbf{P}_1 - f_2(\gamma)\Phi^+(\alpha)), \quad (3.10b)$$

where Ψ^- and Φ^+ are defined as

$$\Psi^-(\alpha) = \int_{-\infty}^0 \psi_-(x)e^{i\alpha x} dx, \quad \Phi^+(\alpha) = \int_0^{\infty} \phi_+(x+l)e^{i\alpha x} dx. \quad (3.11)$$

Assuming that the values of β_{\pm} are known, we can solve (3.6a) and (3.6b) analytically and independently; having done this, we solve an infinite but rapidly convergent system of linear equations to find the values that the β_{\pm} actually take.

3.3. Solution of the integral equations

To solve the two integral equations, they are first transformed into Fourier space where the Wiener–Hopf technique is employed. We begin in §3.3.1 by treating the problem of three uniform plates of potentially different thicknesses. The method used in that problem can be generalized simply to allow either or both of the left- and right-hand plates to be open water. Section 3.3.2 describes how this is done. More significant adjustments to the method of solution are required when the central region contains open water and these are described in §3.3.3.

3.3.1. Solution for three plates

To solve the integral equation (3.6a) using the Wiener–Hopf technique, we must first extend its range to the entire real line. This is done by defining a second function $\psi_+(x)$ that cancels the value that the integral takes for positive x . For negative values of x , it is defined to be identically zero and ψ_- is defined to be zero for positive x . We can now write (3.6a) as

$$\psi_-(x) = \psi_+(x) + H(-x) \sum_{\alpha \in S_1} \beta_+(\alpha)e^{-i\alpha x} + \int_{-\infty}^{\infty} (\mathcal{L}_0 - \mathcal{L}_1)g(x-\xi)\psi_-(\xi) d\xi, \quad (3.12)$$

where $H(x)$ is the Heaviside step function. Analogously, (3.6b) is written

$$\phi_+(x) = \phi_-(x) + H(x) \sum_{\alpha \in S_1} \beta_-(\alpha)e^{i\alpha x} + \int_{-\infty}^{\infty} (\mathcal{L}_0 - \mathcal{L}_1)g(x-\xi)\phi_+(\xi) d\xi. \quad (3.13)$$

Taking the Fourier transforms of (3.12) and (3.13) and rearranging the results yields the following system of Wiener–Hopf equations:

$$\frac{f_0(\gamma)}{f_1(\gamma)}\Psi^-(\alpha) = \Psi^+(\alpha) - i \sum_{k \in S_1} \frac{\beta^+(k)}{\alpha - k}, \quad (3.14a)$$

$$\frac{f_2(\gamma)}{f_1(\gamma)}\Phi^+(\alpha) = \Phi^-(\alpha) + i \sum_{k \in S_1} \frac{\beta^-(k)}{\alpha + k}, \quad (3.14b)$$

where

$$\Psi^+(\alpha) = \int_0^{\infty} \psi_+(x)e^{i\alpha x} dx, \quad \Phi^-(\alpha) = \int_{-\infty}^0 \phi_-(x+l)e^{i\alpha x} dx.$$

Referring back to the definitions of Ψ^- and Φ^+ , if we assume that $\psi_z(x, 0)$ is bounded over the real line or, equivalently, that the displacements of the plates are bounded everywhere, then $\Psi^-(\alpha)$ will be analytic in the lower complex half-plane, $\mathbb{C}^- = \{\alpha \in \mathbb{C} \mid \text{Im}[\alpha] \leq 0\}$, while $\Phi^+(\alpha)$ will be analytic in the upper half-plane, $\mathbb{C}^+ = \{\alpha \in \mathbb{C} \mid \text{Im}[\alpha] \geq 0\}$. Both transforms will also decay at least as fast as $1/|\alpha|$ as $|\alpha| \rightarrow \infty$ in their respective regions of analyticity. Similarly, these assumptions imply

in addition that Ψ^+ is analytic in \mathbf{C}^+ and that Φ_- is analytic in \mathbf{C}^- . (As in the above transforms, a \pm superscript on all subsequent functions will also indicate that the function in question is analytic in \mathbf{C}^\pm .)

Continuing with the Wiener–Hopf solution, our first step is to factorize the quotients f_j/f_1 into products of the form

$$f_j(\gamma)/f_1(\gamma) = K_j^+(\alpha)K_j^+(-\alpha) = K_j^+(\alpha)K_j^-(\alpha).$$

This was done by Chung & Fox (2002*b*), who found the K_j^+ to be

$$K_j^+(\alpha) = \sigma_j \prod_{k' \in S_j} (\alpha + k') \Big/ \prod_{k \in S_1} (\alpha + k), \quad (3.15)$$

where

$$\sigma_j = \prod_{k \in S_1} \gamma(k) \Big/ \prod_{k' \in S_j} \gamma(k') = \sqrt{\frac{D_j}{D_1}}.$$

We can now rearrange (3.14) to give

$$K_0^-(\alpha)\Psi^-(\alpha) + i \sum_{k \in S_1} \frac{\beta^+(k)}{K_0^+(k)(\alpha - k)} = \frac{\Psi^+(\alpha)}{K_0^-(\alpha)} - i \sum_{k \in S_1} \frac{\beta^+(k)}{\alpha - k} \left(\frac{1}{K_0^+(\alpha)} - \frac{1}{K_0^+(k)} \right), \quad (3.16a)$$

$$K_2^+(\alpha)\Phi^+(\alpha) - i \sum_{k \in S_1} \frac{\beta^-(k)}{K_2^+(k)(\alpha - k)} = \frac{\Phi^-(\alpha)}{K_2^-(\alpha)} + i \sum_{k \in S_1} \frac{\beta^-(k)}{\alpha + k} \left(\frac{1}{K_2^-(\alpha)} - \frac{1}{K_2^+(k)} \right). \quad (3.16b)$$

Equation (3.16*a*) is an equality that holds on the real line, with its left-hand side being analytic in \mathbf{C}^- and its right-hand side analytic in \mathbf{C}^+ . Consequently, the Riemann principle implies that both sides are equal to a single entire function. Moreover, when there is no open water present, both sides of (3.16*a*) tend to zero as $|\alpha| \rightarrow \infty$, since in that case the $K_0^\pm(\alpha)$ are $O(1)$ as $|\alpha| \rightarrow \infty$. Therefore, Liouville's theorem implies that the entire function in question is identically zero and so the unknown transform Ψ^- is given by

$$\Psi^-(\alpha) = -i \sum_{k \in S_1} \frac{\beta^+(k)/K_0^+(k)}{K_0^-(\alpha)(\alpha - k)} = -i \sum_{k \in S_0} \frac{a(\alpha)}{\alpha - k}. \quad (3.17)$$

Similar reasoning applied to (3.16*b*) provides the result

$$\Phi^+(\alpha) = i \sum_{k \in S_1} \frac{\beta^-(k)/K_2^+(k)}{K_2^+(\alpha)(\alpha - k)} = i \sum_{k \in S_0} \frac{d(\alpha)}{\alpha + k}. \quad (3.18)$$

The a and d coefficients in the above two equations are given by

$$a(\alpha) = i \operatorname{Res}[\Psi^-(k), k = \alpha] = \sum_{k \in S_1} M_a(\alpha, k)\beta_+(k), \quad (3.19a)$$

$$d(\alpha) = -i \operatorname{Res}[\Phi^+(k), k = -\alpha] = \sum_{k \in S_1} M_d(\alpha, k)\beta_-(k), \quad (3.19b)$$

where

$$M_a(\alpha, k) \Big|_{\alpha \in S_0} = \frac{A_0(\alpha)f_1(\gamma)K_0^+(\alpha)}{K_0^+(k)(\alpha - k)}, \quad (3.20a)$$

$$M_d(\alpha, k) \Big|_{\alpha \in S_2} = \frac{A_2(\alpha)f_1(\gamma)K_2^+(\alpha)}{K_2^+(k)(\alpha - k)}, \quad (3.20b)$$

for $k \in S_1$.

The two transforms Ψ^- and Φ^+ can now be inverted to give us explicit expressions for $\psi_-(x)$ and $\phi_+(x)$, as follows:

$$\psi_-(x) = \sum_{\alpha \in S_0} a(\alpha) e^{-i\alpha x}, \quad \phi_+(x) = \sum_{\alpha \in S_2} d(\alpha) e^{i\alpha(x-l)}, \quad (3.21a,b)$$

and the limit as $\varepsilon \rightarrow 0$ can be taken. Accordingly, the scattering coefficients R and T are given by

$$R = a(\alpha_0)/\varphi_0'(0), \quad T = d(\alpha_2)e^{-i\alpha_2 l}/\varphi_2'(0).$$

However, the solution is not yet complete, as R and T , and indeed all the a and d coefficients, still depend on the unknown coefficients β_{\pm} in (3.8), which themselves depend on the b and c coefficients (3.10). Nonetheless, it is apparent that only a few of the b and c are needed, as $\beta_+(\alpha) \propto c(\alpha) \exp(i\alpha l)$ and $\beta_-(\alpha) \propto b(\alpha) \exp(i\alpha l)$, and most of the $\alpha \in S_1$ have large positive imaginary parts.

For $\alpha \in S_1$, we can calculate $\Psi^-(-\alpha)$ from (3.17) and $\Phi^+(\alpha)$ from (3.18) and substitute them into equations (3.10a) and (3.10b). This gives a system of linear equations of the form

$$b(\alpha) = f_b(\alpha) + \sum_{k \in S_1} M_b(\alpha, k) \beta_+(k), \quad (3.22a)$$

$$c(\alpha) = f_c(\alpha) + \sum_{k \in S_1} M_c(\alpha, k) \beta_-(k). \quad (3.22b)$$

Again, the b coefficients depend only on a few of the c coefficients and vice versa. We may now eliminate the $c(\alpha)$ from (3.22a), find the required number of $b(\alpha)$, and then generate the $a(\alpha)$, $c(\alpha)$ and $d(\alpha)$.

All that remains is to find the unknown vectors \mathbf{P}_0 and \mathbf{P}_l by applying the appropriate edge conditions. This will be described in §4.3.

3.3.2. Solution for a VLFS or a breakwater

When either h_0 or h_2 is zero, then the corresponding set S_j will not contain the two complex roots described in §3.1. The main consequence of this is that the factor σ_j in (3.15) formally evaluates to

$$\sigma_j = \sqrt{\frac{\lambda}{D_1}},$$

although its convergence to this number is slow and the original definition in terms of the products of the roots appears to work better.

Asymptotically, the absence of the complex roots means that $|K_j^+(\alpha)| \sim O(|\alpha|^{-2})$ as $|\alpha| \rightarrow \infty$. This implies that the right-hand side of the relevant equation in (3.16) is potentially $O(|\alpha|)$ as $|\alpha| \rightarrow \infty$. However, the left-hand side will be at most $O(|\alpha|^{-3})$ and so both sides must still be equal to zero.

Hence, (3.17)–(3.22) still hold and our solution is complete once we have applied the appropriate edge conditions.

3.3.3. Solution for an open lead

When $h_1 = 0$, $g(x)$ has a logarithmic singularity at the origin and so the derivatives of that function required in (3.6) are highly singular. In theory, all singularities should be cancelled out, but the solution proceeds more smoothly when they are removed explicitly.

By integrating by parts, the system (3.6) can be rewritten as

$$\begin{aligned} \psi_-(x) = \sum_{\alpha \in S_1} c(\alpha) e^{i\alpha(l-x)} - \int_0^\infty (\mathcal{L}_0 - \lambda) \phi_{0,z}(\xi, 0) g(x - \xi) d\xi \\ + \int_{-\infty}^0 (\mathcal{L}_0 - \lambda) \psi_-(\xi) g(x - \xi) d\xi, \end{aligned} \quad (3.23a)$$

$$\phi_+(x) = \sum_{\alpha \in S_1} b(\alpha) e^{i\alpha x} + \int_l^\infty (\mathcal{L}_2 - \lambda) \phi_+(\xi) g(x - \xi) d\xi, \quad (3.23b)$$

where $\phi_c(x)$ can still be written as in (3.9), but the b and c coefficients are now given by

$$b(\alpha) = f_1(\gamma_0) \phi'_0(0) \frac{A_1(\alpha)}{\alpha_0 - \alpha} - A_1(\alpha) \sum_{k \in S_0} \frac{a(k) f_1(\kappa)}{\alpha + k}, \quad (3.24a)$$

$$c(\alpha) = -A_1(\alpha) \sum_{k \in S_2} \frac{d(k) f_1(\kappa)}{\alpha + k}, \quad (3.24b)$$

where $\kappa = \gamma(k)$. Proceeding in much the same way as in §3.3.1, we take the Fourier transforms of (3.23a) and (3.23b) and rearrange to give

$$\Psi^-(\alpha) = \frac{i\phi'_0(0)}{\alpha + \alpha_0} + \frac{\mathbf{p}^T(\alpha) \mathbf{P}_0}{f_0(\gamma)} - \frac{f_1(\gamma)}{f_0(\gamma)} \left(\Psi^+(\alpha) + i \sum_{k \in S_1} \frac{c(k) e^{ikl}}{\alpha - k} \right), \quad (3.25a)$$

$$\Phi^+(\alpha) = \frac{\mathbf{p}^T(\alpha) \mathbf{P}_l}{f_2(\gamma)} - \frac{f_1(\gamma)}{f_2(\gamma)} \left(\Phi^-(\alpha) - i \sum_{k \in S_1} \frac{b(k) e^{ikl}}{\alpha + k} \right). \quad (3.25b)$$

These transforms can be inverted to put the a and d coefficients in terms of b and c , giving

$$a(\alpha)|_{\alpha \in S_0} = iA_1(\alpha)(\mathbf{p}^T(\alpha) \mathbf{P}_0 - f_1(\gamma) \beta_+(\alpha)), \quad (3.26a)$$

$$d(\alpha)|_{\alpha \in S_2} = iA_2(\alpha)(\mathbf{p}^T(-\alpha) \mathbf{P}_l - f_1(\gamma) \beta_-(\alpha)), \quad (3.26b)$$

where

$$\beta_+(\alpha) = \Psi^+(\alpha) + i \sum_{k \in S_1} \frac{c(k) e^{ikl}}{\alpha - k}, \quad \beta_-(\alpha) = \Phi^-(\alpha) + i \sum_{k \in S_1} \frac{b(k) e^{ikl}}{\alpha - k}.$$

Were it not for the presence of the unknown transforms Ψ^+ and Φ^- in the formulae for the a and d coefficients (3.26), we could eliminate those sets of coefficients from (3.24) and solve for $b(\alpha)$ and $c(\alpha)$ as we did in §§3.3.1 and 3.3.2.

However, to find the b and c coefficients we must also find a way to write Ψ^+ and Φ^- in terms of them as well. This is done by using the Wiener–Hopf technique to solve (3.25) in the same way that we solved (3.16) in §3.3.1 although, as in §3.3.2 when either h_0 or h_2 is zero, we must first adjust our formulae for the K_j^+ functions. In this case, the σ_j factors formally evaluate to $(D_j/\lambda)^{1/2}$, but they are again best evaluated as the original product of roots. Asymptotically, $|K_j^+(\alpha)| \sim O(|\alpha|^2)$ as $|\alpha| \rightarrow \infty$.

Proceeding with the solution, we are finally able to write the following expressions for Ψ^+ and Φ^- :

$$\Psi^+(\alpha) = K_0^+(\alpha) \left(i\phi'_0(0) \frac{K_0^+(\alpha_0)}{\alpha + \alpha_0} - \sum_{k \in S_0} \frac{A_0(k) \mathbf{p}^T(-k) K_0^+(k)}{\alpha + k} \mathbf{P}_0 \right) - i \sum_{k \in S_1} \frac{c(k) e^{ikl}}{\alpha - k} \left(1 - \frac{K_0^+(\alpha)}{K_0^+(k)} \right), \quad (3.27a)$$

$$\Phi^-(\alpha) = K_2^-(\alpha) \sum_{k \in S_2} \frac{A_2(k) \mathbf{p}^T(k) K_2^+(k)}{\alpha - k} \mathbf{P}_l + i \sum_{k \in S_1} \frac{b(k) e^{ikl}}{\alpha + k} \left(1 - \frac{K_2^-(\alpha)}{K_2^+(k)} \right). \quad (3.27b)$$

The $\beta_{\pm}(\alpha)$ can now be eliminated from (3.26), which allows us to remove the a and d from (3.24) and, after applying the edge conditions using the method described in §4.3, the solution follows as in §3.3.1.

4. Residue calculus solution

Here we confirm the results of §§3.3.1 and 3.3.2 using the residue calculus technique (Linton & McIver 2001, §5.2). We were not successful in reproducing the Wiener–Hopf results of §3.3.3 for the open lead problem analytically, although this is not to say that residue calculus cannot be used for that situation, as Chung & Linton (2005) showed. However, our Wiener–Hopf results for an open lead can still be checked numerically using the method of Williams (2006, chap. 7), which is also presented in Williams & Squire (2006). This is done in §5.2.

The method of this section begins by applying (2.2c) at $x=0$ and $x=l$. This leads to an infinite system of linear equations that may be simplified by using residue calculus to invert two matrices analytically. This simpler set of equations is exactly the same as (3.22) and its solution requires far fewer (less than half) unknown coefficients to be found than did the original system.

4.1. Derivation of mode-matching equations

We show in the Appendix that Green’s theorem implies $\phi(x, z)$ can be expanded as

$$\phi(x, z) = \begin{cases} \phi_0(x, z) + \sum_{\alpha \in S_0} \hat{a}(\alpha) e^{-i\alpha x} \varphi(z, \alpha) & \text{for } x < 0, \\ \sum_{\alpha \in S_1} (\hat{b}(\alpha) e^{i\alpha x} + \hat{c}(\alpha) e^{i\alpha(l-x)}) \varphi(z, \alpha) & \text{for } 0 < x < l, \\ \sum_{\alpha \in S_2} \hat{d}(\alpha) e^{i\alpha(x-l)} \varphi(z, \alpha) & \text{for } x > l. \end{cases} \quad (4.1)$$

The coefficients in the above expansions are related to the a, b, c and d coefficients of the previous section by

$$a(\alpha) = \hat{a}(\alpha) \varphi_z(0, \alpha), \quad b(\alpha) = \hat{b}(\alpha) \varphi_z(0, \alpha), \quad c(\alpha) = \hat{c}(\alpha) \varphi_z(0, \alpha) \quad d(\alpha) = \hat{d}(\alpha) \varphi_z(0, \alpha).$$

Observe that the two conditions contained in (2.2c) are equivalent to requiring that the functions $\phi_{\pm}(x, z) = i\alpha\phi(x, z) \pm \phi_x(x, z)$ are continuous everywhere in the fluid for $\alpha \neq 0$. Using the expansion (4.1) in ϕ_{\pm} will provide automatic continuity for all x , except at $x=0$ and $x=l$ where continuity must be applied explicitly. At $x=0$, we require that

$$\begin{aligned}
 i(\alpha \pm \alpha_0)\varphi_0(z) + i \sum_{k \in S_0} (\alpha \mp k)\hat{a}(k)\varphi(z, k) \\
 = i \sum_{k \in S_1} ((\alpha \pm k)\hat{b}(k) + (\alpha \mp k)\hat{c}(k)e^{ikl})\varphi(z, k), \quad (4.2)
 \end{aligned}$$

while at $x = l$, we require that

$$i \sum_{k \in S_2} (\alpha \mp k)\hat{d}(k)\varphi(z, k) = i \sum_{k \in S_1} ((\alpha \pm k)\hat{b}(k)e^{ikl} + (\alpha \mp k)\hat{c}(k))\varphi(z, k). \quad (4.3)$$

Now, by adjusting the rules of Lawrie & Abrahams (1999), we have the following integral rules: if $\alpha \in S_i$ and $k \in S_j$, then if $i \neq j$

$$\int_0^H \frac{\varphi(z, \alpha)\varphi(z, k) dz}{\varphi_z(0, \alpha)\varphi_z(0, k)} = \frac{f_j(\gamma)}{k^2 - \alpha^2} - D_j(\gamma^2(\alpha) + \gamma^2(k)), \quad (4.4)$$

whereas if $i = j$, then

$$-2\alpha A_j(\alpha) \int_0^H \frac{\varphi(z, \alpha)\varphi(z, k) dz}{\varphi_z(0, \alpha)\varphi_z(0, k)} = \delta_{\alpha, k} + 2\alpha D_j A_j(\alpha)(\gamma^2(\alpha) + \gamma^2(k)). \quad (4.5)$$

Note that (4.5) may be derived from (4.4) by taking the limit as $f_j \rightarrow f_i$.

Consequently, multiplying (4.2) by $\varphi(z, \alpha)$ with $\alpha \in S_1$, integrating with respect to z from 0 to H and simplifying, yields

$$b(\alpha) = iA_1(\alpha)F_0(-\alpha) + A_1(\alpha)f_0(\gamma) \sum_{k \in S_0} \frac{a(k)}{\alpha + k}, \quad (4.6a)$$

$$c(\alpha)e^{i\alpha l} + iA_1(\alpha)F_0(\alpha) = A_1(\alpha)f_0(\gamma) \sum_{k \in S_0} \frac{a(k)}{\alpha - k}. \quad (4.6b)$$

Recalling that $\Psi^-(\alpha) = -i \sum_{k \in S_0} a(k)/(\alpha - k)$, (4.6a) is equivalent to (3.10a). Equation (3.19a) is derived in the next section by using residue calculus to solve (4.6b) for the $a(k)$ in terms of the $c(\alpha)$. In passing, we note also that the left-hand side of (4.6b) is $\beta_+(\alpha)$.

The analogous set of equations to (4.6) follows from (4.3) in a similar fashion, and is

$$c(\alpha) = iA_1(\alpha)\mathbf{p}^T(\alpha)\mathbf{P}_l + A_1(\alpha)f_2(\gamma) \sum_{k \in S_2} \frac{d(k)}{\alpha + k}, \quad (4.7a)$$

$$b(\alpha)e^{i\alpha l} + iA_1(\alpha)\mathbf{p}^T(-\alpha)\mathbf{P}_l = A_1(\alpha)f_2(\gamma) \sum_{k \in S_2} \frac{d(k)}{\alpha - k}, \quad (4.7b)$$

where $\alpha \in S_1$ again. Also, since $\Phi^+(\alpha) = i \sum_{\alpha \in S_2} d(k)/(\alpha + k)$, (4.7a) and (3.10b) are equivalent. And, like (4.6b), (4.7b) can be solved for the $d(k)$ using residue calculus to reproduce equations (3.19b). Here, the left-hand side of (4.6b) is $\beta_-(\alpha)$. The details of the inversion of (4.6b) are given in the following section; the inversion of (4.7b) proceeds in exactly the same way and so is not presented.

4.2. Solution of the residue calculus equations

To solve (4.6b), we look for an infinite matrix $M_a(\alpha, k')$ such that for $\alpha, k \in S_0$

$$\sum_{k' \in S_1} M_a(\alpha, k') \frac{A_1(k')(\kappa')}{k - k'} = -\delta(\alpha, k), \quad (4.8)$$

where $\alpha, k \in S_0$ and $\kappa' = \gamma(k')$, and

$$\delta(\alpha, k) = \begin{cases} 1 & \text{if } \alpha = k, \\ 0 & \text{if } \alpha \neq k. \end{cases} \tag{4.9}$$

Equation (4.6*b*) would then imply that

$$a(\alpha) = \sum_{k' \in S_1} M_a(\alpha, k') \beta_+(k'), \tag{4.10}$$

and (3.19*a*) would be verified.

An alternative way of formulating (4.11) is to look for a function $f(\alpha, k)$ that vanishes as $|\alpha| \rightarrow \infty$, is meromorphic in α , with poles when $\alpha \in S_1$, and that satisfies

$$f(\alpha, k) = -\delta(\alpha, k) \quad \text{for } \alpha, k \in S_0. \tag{4.11}$$

For each value of $k \in S_0$, the function $f(\alpha, k)$ will then have a partial fractions expansion of the same form as the left-hand side of (4.8). Equating the coefficients gives us

$$M_a(k, k') A_1(k') f_0(k') = \text{Res}[f(\alpha, k), \alpha = k' \in S_1]. \tag{4.12}$$

From our Wiener–Hopf working, as long as $h_1 \neq 0$, a suitable candidate for $f(\alpha, k)$ is

$$f(\alpha, k) = -A_0(k) f_1(\kappa) K_0^+(\kappa) \frac{K_0^-(\alpha)}{\alpha - k} = -\frac{f_1(\kappa) K_0^+(\kappa) A_0(k) f_0(\gamma)}{f_1(\gamma) K_0^+(\alpha) \alpha - k}. \tag{4.13}$$

(Recall that if $h_1 = 0$, then $|K_0^+(\alpha)| \sim O(|\alpha|^2)$ as $|\alpha| \rightarrow \infty$, making $f(\alpha, k) \sim O(|\alpha|)$. As a consequence, its partial fractions expansion would have to include a linear function as well as a sum over its poles.) Hence, as in (3.20),

$$M_a(\alpha, k) = \frac{A_0(\alpha) f_1(\gamma) K_0^+(\alpha)}{K_0^+(k)(\alpha - k)}. \tag{4.14}$$

Thus, in this section we have shown that the $a(\alpha)$ depend on the $c(\alpha)$ in exactly the same way as they did in §3.3 (cf. equation (3.19*a*)). By applying the same procedure to (4.7*b*), we can also show that the $d(\alpha)$ depend on the $b(\alpha)$ in the manner prescribed by (3.19*b*).

In addition, since we also showed that equations (4.6*a*) and (4.7*a*) were the same as (3.10*a*) and (3.10*b*), using (3.19*a*) and (3.19*b*) to eliminate the $a(\alpha)$ and $d(\alpha)$ from the system of equations will inevitably produce (3.22). Therefore, the $b(\alpha)$ and $c(\alpha)$ will be the same as in §3.3 and so will $a(\alpha)$, $d(\alpha)$, R and T .

4.3. Application of the edge conditions

The last step in the solution, which is common to both the Wiener–Hopf solution and the residue calculus solution, is the application of the edge conditions. Since our a, b, c and d coefficients still depend on the unknown vectors \mathbf{P}_0 and \mathbf{P}_l , we must find them by applying either (2.3) or (2.4) as described below.

If we wish to apply the fixed-edge conditions, we substitute (2.3) into the definitions of the unknown \mathbf{P}_{x_e} vectors to give

$$\mathbf{P}_{x_e} = (D(x_e^+) - D(x_e^-)) \begin{pmatrix} \phi_z(x_e^\pm) \\ \phi_{zx}(x_e^\pm) \\ 0 \\ 0 \end{pmatrix}.$$

We may evaluate the $\partial_x^j \phi_z(x_e^\pm)$ using either (3.9) or one of (3.21*a,b*), or equivalently using the expansion for the relevant region in (4.1); we may choose whether to take the right-hand or left-hand limit according to whichever is most convenient.

For a free edge, we first apply (2.3*c*) and (2.3*d*), making $[\mathbf{P}_{x_e}]_3 = [\mathbf{P}_{x_e}]_4 = 0$, as was the case when we applied the free-edge conditions. We then apply (2.4), again substituting in either (3.9) or (3.21*a,b*), or equivalently (4.1). When there are plates on both sides of the edge in question, we are able to choose whether to take the right-hand or left-hand limits. This is because we have already applied (2.3*c*) and (2.3*d*).

However, if the edge separates a plate from another region of open water, then we must take the limit from within the plate. This might seem surprising, as in this case applying (2.3*c*) and (2.3*d*) is exactly the same as applying (2.4). ($D(x)=0$ in a region of open water.) However, the Green's function that we used did not satisfy the adjoint edge conditions, so applying the edge conditions a second time is equivalent to applying the adjoint conditions.

5. Results

We begin this section by validating the theory developed above. This is done in two ways: first, by demonstrating that predictions are well-behaved and sensible, particularly in limiting cases; and secondly, by comparing results that arise in simpler situations with the more restrictive, alternative models that have been published previously (see § 1), especially for waves propagating beneath continuous ice sheets. In addition, a conservation of energy relationship between the reflection and transmission coefficients (Fox & Squire 1990) was used to provide further confirmation of our results.

Physical parameters used in this section are $E_j = 5 \times 10^9$ Pa, $\nu_j = 0.3$, $\rho_j = 922.5 \text{ kg m}^{-3}$ (for $j = 0, 1, 2$), $\rho = 1025 \text{ kg m}^{-3}$ and $g = 9.81 \text{ m s}^{-2}$. In order to concentrate on the effect of other parameters, we will present only infinite-depth results. Williams (2006) showed that these could be obtained by setting the non-dimensional water depth to 5. If the free-edge conditions are applied at this water depth, about eighty evanescent modes are required for convergence to graphical precision at the lowest period used (2 s), whereas fewer than thirty are required for the highest period (20 s). Only fifty modes are necessary when the frozen-edge conditions are applied at the lowest period.

5.1. Validation

In figure 2, the reflection coefficient is plotted for refrozen leads of two different widths and four different thicknesses, in each case welded to the surrounding 1 m thick sea-ice. The full, i.e. accurate, solution is shown by a solid line, while an approximate one that neglects the evanescent modes is shown by a dashed line. Notice that the overall level of reflection increases from top to bottom, i.e. from figure 2(*a*) to 2(*c*) to 2(*e*) to 2(*g*) as σ decreases, etc., which is expected because the feature becomes more prominent as its ice becomes thinner. Also notice that the fine structure in the curves is least for the left-hand set and greatest for the right-hand set, which correspond to lead widths of 15 m and 50 m, respectively. This is because interference effects are more likely within the band of typically observable wave periods for wider leads, where they can lead to perfect transmission, i.e. zeros in the reflection coefficient, at certain periods. Moreover, since the wavelength in ice increases monotonically with thickness, the number of zeros increases from top to bottom as σ decreases and the

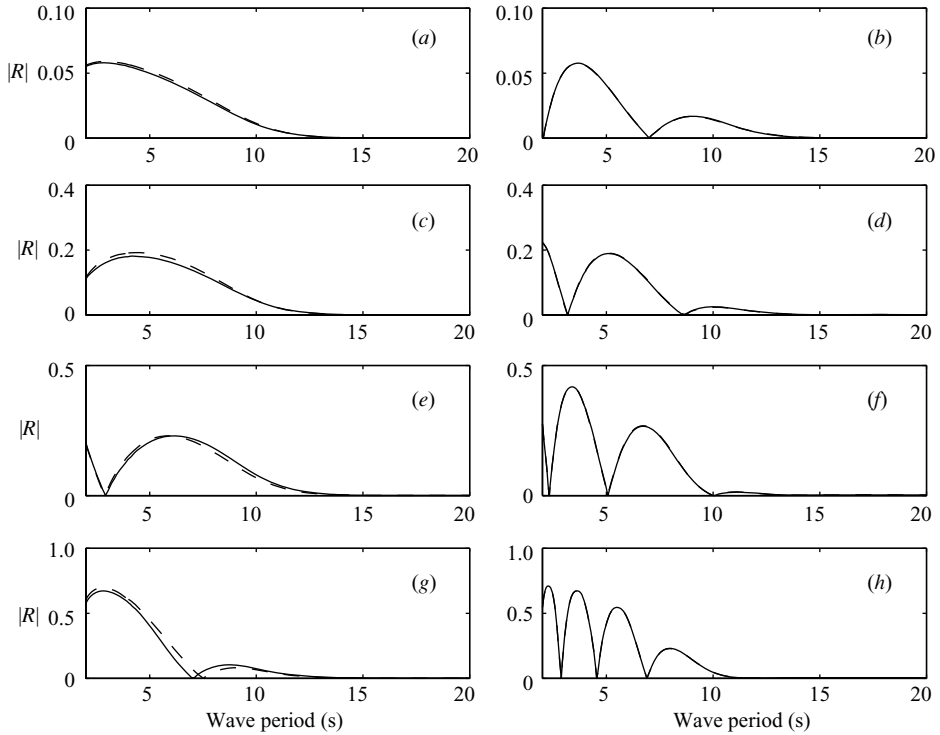


FIGURE 2. The reflection coefficient for normal incidence arising from a refrozen lead containing ice that is welded to the surrounding sea-ice sheets, i.e. satisfies (2.3), which in this case are of equal thickness $h_0 = h_2 = 1$ m. The lead width in the left-hand plots (a, c, e, g) is $l = 15$ m while $l = 50$ m in the right-hand plots (b, d, f, h). Ice thickness in the lead itself is $h_1 = 0.9\sigma h_0$, where $\sigma = 1$ (a, b), $\sigma = 3/4$ (c, d), $\sigma = 1/2$ (e, f), $\sigma = 1/4$ (g, h). In each case, the solid line represents the accurate solution while the dashed line is an approximate one found by neglecting the contribution from the evanescent waves. For the welded-edge situation shown here, the agreement is quite good at all thicknesses and improves with the width of the lead, where the dashed curve is obscured by the solid one.

ice in the lead becomes thinner. The solid curves presented reproduce precisely those of Williams & Squire (2004b, figure 5a), which were obtained using a simpler model.

Figure 3 is equivalent to figure 2 for the free-edge conditions (2.4). In this case σ varies from 1, $2/3$, $1/3$ and 0 from top to bottom and the widths are 15 m and 50 m as before. Fine structure is much more evident here, both for the narrow leads and especially for the wider ones where many zeros in the reflection coefficient occur. The open-water lead plots, figures 3(g) and 3(h), reproduce the behaviour shown in figure 3 of Chung & Linton (2005), although there the curves are plotted as a function of the radial frequency ω (nondimensionalized using the same scheme as here), rather than wave period. Specific plots in figure 3 of the current paper are also convincingly similar to those of Squire & Dixon (2001b), although the lead widths are different.

In figure 4, we show how the reflection coefficient varies for a plate of thickness 1 m in open water and surrounding thin ice (figure 4a, b); and plates of different thickness embedded in 1 m thick sea-ice (figure 4c, d). This is done against the wave period on the left-hand plots and against the width of the plate on the right-hand side. The

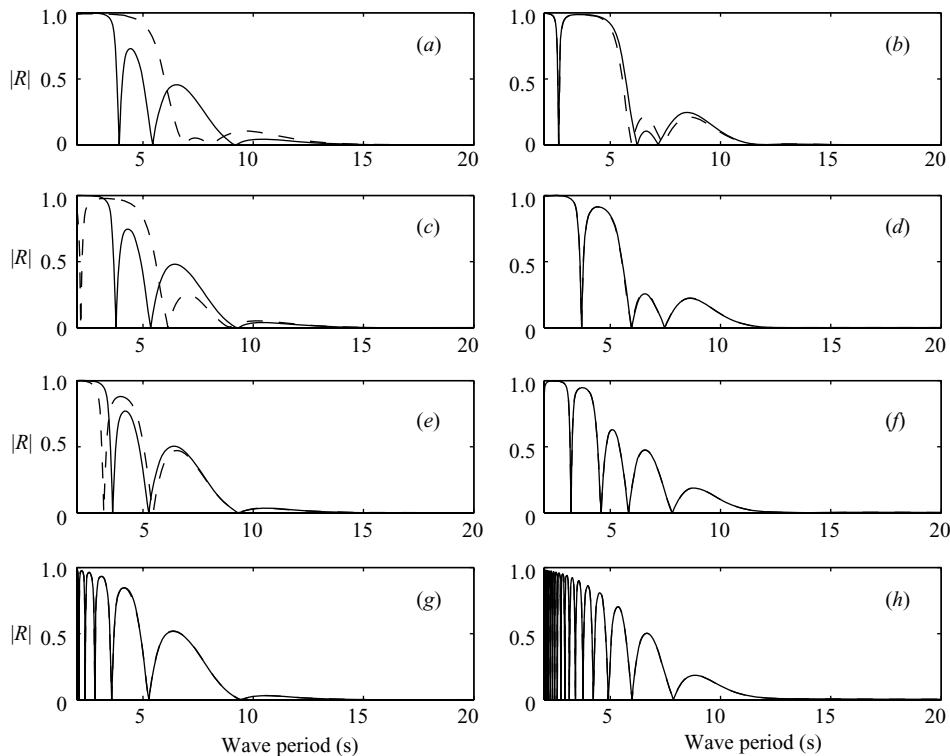


FIGURE 3. The reflection coefficient for normal incidence arising from an open-water lead or a refrozen lead containing ice that is unattached to the surrounding sea-ice sheets, i.e. satisfies (2.4), which in this case are of equal thickness $h_0 = h_2 = 1$ m. The lead width in the left-hand plots (a, c, e, g) is $l = 15$ m while $l = 50$ m in the right-hand plots (b, d, f, h). Ice thickness in the lead itself is $h_1 = 0.9\sigma h_0$, where $\sigma = 1$ (a, b), $\sigma = 2/3$ (c, d), $\sigma = 1/3$ (e, f), $\sigma = 0$ (g, h). In each case, the solid line represents the accurate solution while the dashed line is an approximate one found by neglecting the contribution from the evanescent waves. For the free-edge situation shown here, the best agreement occurs when the lead ice is thinnest or absent and the lead is wide. (In these cases the solid curve obscures the dashed ones.)

open-water plot (solid line in figure 4a) is the same as plotted by Meylan (1993) using an entirely different method based primarily on Green's theorem. Figures 4(b) and 4(c) are identical to those of figures 3 and 4 of Squire & Dixon (2001b), again found using a Green's function approach. The curves in figures 4(b) and 4(d) illustrate, for an 8 s wave, how zero reflection can occur at certain plate widths. Focusing on figure 4(d), for example, the wavelengths corresponding to 8 s for each plate thickness are 1 m: 124 m (solid); 2 m: 165 m (dashed); 5 m: 261 m (dot-dashed); and 10 m: 380 m. Once the plate is wide enough for the evanescent contributions to be neglected, the zeros are roughly commensurate with the half-wavelength, in agreement with earlier work (Meylan 1993; Squire & Dixon 2001b).

5.2. Geophysical results

We begin this section by providing in figure 5(a, b) some results when the thickness $h_0 \neq h_1 \neq h_2$. The plots also demonstrate that the model described earlier converges to the same solution as those found by an entirely different method using numerical integration (see Williams 2006, chap. 7; Williams & Squire 2006). Results are

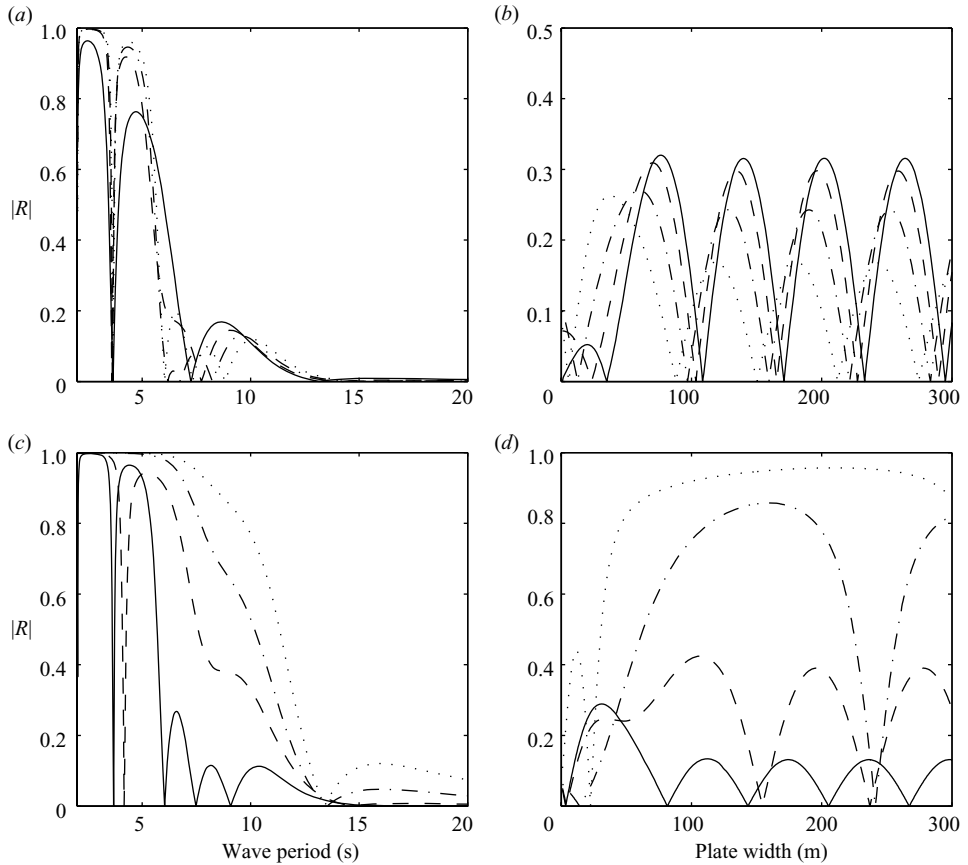


FIGURE 4. The reflection coefficient arising from an ice plate that is unattached to the surrounding identical sea-ice sheets, plotted against the period for a plate width of 100 m (*a, c*) and against the width of the plate (*b, d*) for 8 s period waves. In (*a*) and (*b*), $h_0 = h_2 = 0$ (solid), 0.5 m (dashed), 0.7 m (dot-dashed), 0.9 m (dotted) and $h_1 = 1$ m; in (*c*) and (*d*), $h_0 = h_2 = 1$ m and $h_1 = 1$ m (solid), 2 m (dashed), 5 m (dot-dashed), 10 m (dotted). The curves in (*c*) are identical to those in figure 4 of Squire & Dixon (2001*a*), found by an entirely different method.

reassuringly identical, including when $h_1 = 0$ in the solid curves of figure 5(*b, d*). (Recall that we could not confirm the Wiener–Hopf results for an open lead analytically.) The phases, which are not plotted, were also checked and found to be in similar agreement. In terms of their trend and fine structure, the results are superficially similar to those when the thicknesses on either side of the enclosed region are the same, except that the zeros that arise because of interference become non-zero minima.

A further application of the model is provided in figures 6 and 7. Although we have until now regarded the theory as being applicable to three adjoining continuous ice sheets of thicknesses h_0 , h_1 and h_2 , respectively (recalling that any of the three thicknesses can also be zero), by patching many of these sets of three sheets together, we can fashion a theoretical analogue of an entire polar ice cover that allows spatial variability. Both open and refrozen leads of any width can be modelled, as can simple changes of thickness. Although pressure ridges would generally be more complicated in terms of their cross-sectional shape, the model affords an approximate method

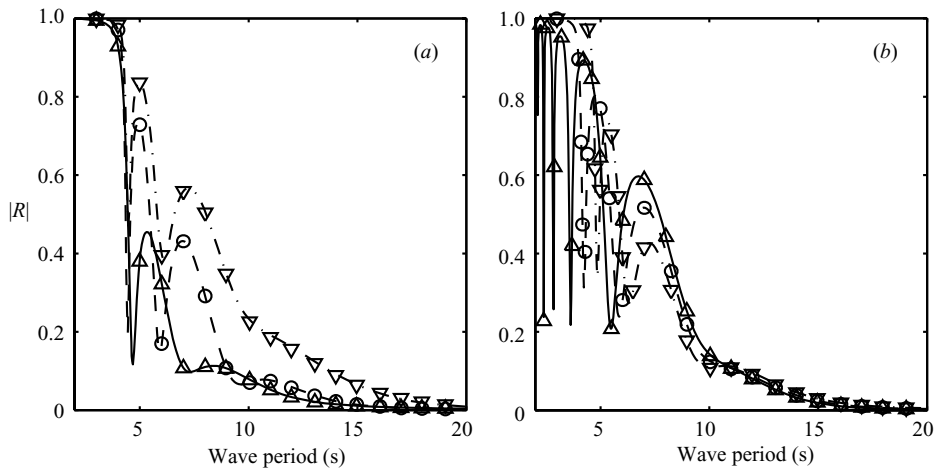


FIGURE 5. The reflection experienced by ice-coupled waves as they propagate from a sea-ice sheet of thickness h_0 across a free ice plate of width 15 m and thickness $h_1 \neq h_0$ into a second semi-infinite sheet of thickness $h_2 \neq h_1 \neq h_0$. In (a), $h_0 = 0$ (solid, Δ), 1.5 m (dashed, \odot), 3 m (dot-dashed, ∇), $h_1 = 2$ m and $h_2 = 1$ m; in (b) $h_0 = 1$ m, $h_1 = 0$ (solid, Δ), 1.5 m (dashed, \odot), 3 m (dot-dashed, ∇) and $h_2 = 2$ m. The curves in each plot are computed by the method of the current paper, while the points are computed using numerical integration coupled with a single Wiener–Hopf equation (Williams 2006).

of dealing with these also, recognizing that at short periods, the draft of these irregularities may be significant enough for the assumption of zero submergence to become untenable.

Equally, the model can be regarded as applicable to the marginal ice zone (MIZ), as a continuous sheet of ice interlaced by leads can likewise be interpreted as a number of discrete ice floes separated by open water, recalling again that the solution developed in §3 allows for arbitrary floe thickness and width. To the far left of the floes is a semi-infinite region of open ocean, while to their far left is a semi-infinite region of shore-fast ice. This ice will have the same thickness as the mean ice thickness of the floes in the MIZ. The results of doing this can then be compared directly with those reported by Kohout & Meylan (2006), which are computed using an entirely different method based on matching eigenfunctions at the edges of the constituent ice floes that make up the MIZ. The computational approach that we take is to calculate the scattering by the single floes and by the semi-infinite sheet on the right exactly, but to take advantage of the smaller wavelength and rapid decay of the evanescent waves in open water by using the wide-spacing approximation to combine the results for the individual floes. We could also have made a further wide-spacing approximation to compute the scattering for the individual floes, but the wavelength in the ice is much longer than in open water and we would have lost some accuracy in our calculations for smaller floe widths. (For example, referring again to figure 3b, there are still noticeable differences between the exact results and the approximate wide-spacing ones when the central strip is 0.9 m thick and 50 m wide.)

Our first simulation of the MIZ is shown in figure 6. We have constructed an MIZ made up of 10, 20, 50 and 100 floes with a fixed floe size of 50 m and a fixed separation of 30 m; obviously, this is a very simple marginal ice zone, but it allows us to show how the reflection coefficient (figure 6a–d) changes with wave period. As

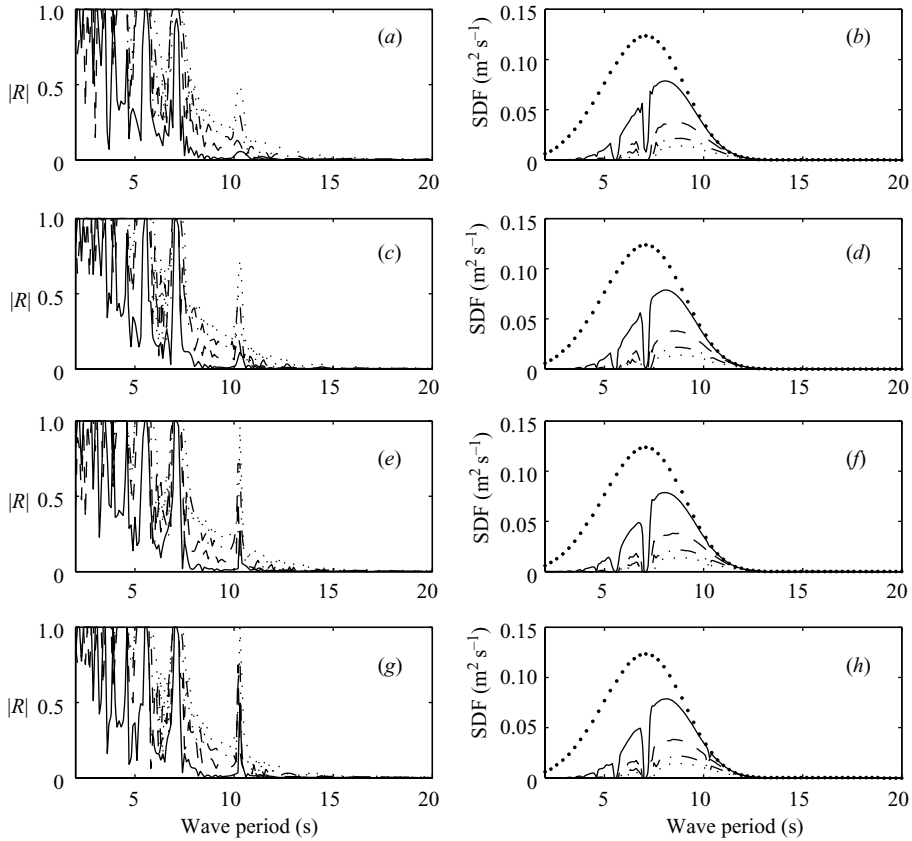


FIGURE 6. The scattering by N identical floes in an MIZ. The graphs in the left-hand column plot $|R|$ against the period, while the right-hand graphs denote transmitted spectra for an incident Pierson–Moskowitz spectrum (also shown as the closely spaced dotted curve that envelopes the others). The floes have thickness h_1 , are 50 m wide and are spaced 30 m apart. They are located between a semi-infinite region of open water and a semi-infinite region of ice that also has thickness h_1 . Solid curves correspond to $h_1 = 0.5$ m, dashed to 1 m, dot-dashed to 1.5 m and dotted to 2 m. (a, e) correspond to $N = 10$, (b, f) to $N = 20$, (c, g) to $N = 50$, and (d, h) to $N = 100$.

well as the expected gradual decrease in reflection coefficient as period increases, the curves in figure 6(a–d) have considerable fine structure owing to the integrated effect of the zeros discussed earlier in the context of reflection from a single feature. The fine structure arises because of the coherent nature of the simulation, which has all floes identical in terms of thickness, width and separation. Of greater geophysical importance, figure 6 illustrates how a Pierson–Moskowitz power spectrum of incident wave periods (Pierson & Moskowitz 1964) is altered by a simple configuration of ice floes (figure 6e–h) because of this complexity. Note that although such a spectrum is usually presented as a function of frequency, we have defined it in terms of period for ease of comparison with our reflection results. At certain periods (\dots , ~ 3.9 s, 5.5 s, 7.1 s, 10.3 s, \dots , for example), the ice field can block the passage of waves completely because its uniformity produces perfectly coherent interactions between the incoming and multiply reflected waves at each period. Although it is also common

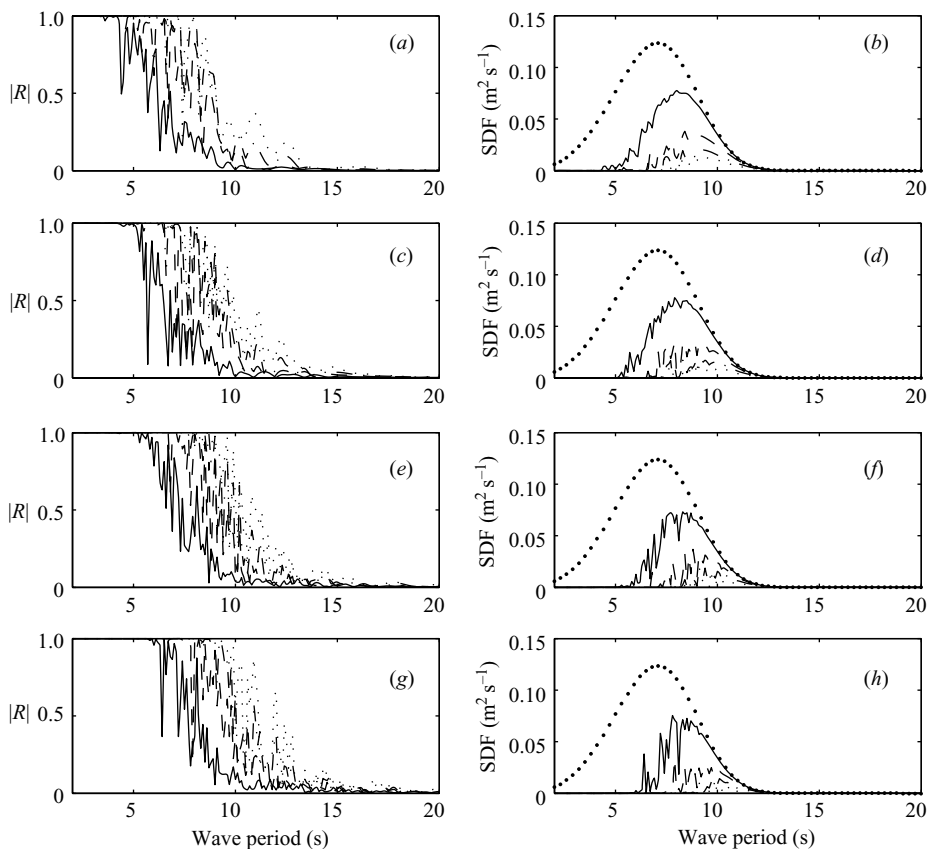


FIGURE 7. The scattering by N ice floes of random thickness, random width and random separation in an MIZ. (Results apply to a single realization of the statistical distributions for these properties.) The graphs in the left-hand column show $|R|$ against period, while the right-hand graphs show the transmitted spectra arising from an incident Pierson–Moskowitz spectrum (shown again as the enveloping, closely-spaced dotted curve). The floes have a mean thickness centred on $h_1 = 0.5$ m (solid), 1 m (dashed), 1.5 m (dot-dashed) and 2 m (dotted). They are located between a semi-infinite region of open water and another semi-infinite region of ice that also has thickness h_1 . As in figure 6, $N = 10$ in (7a, e), $N = 20$ (b, f), $N = 50$ (c, g) and $N = 100$ (d, h).

for such regular arrangements to produce periods of complete transmission, this is not observed here because of the difference in ice thicknesses to the far left and right of the MIZ. Recall that this was apparent in figure 5 when h_0 and h_2 were different.

It is clear that the ice thickness has a very significant effect on the evolution of the wave spectrum as it travels through the pack ice: note the substantial difference between the solid, dashed, dot-dashed and dotted curves in figure 6(e–h), for example. In contrast, while there is certainly some modification of the spectra between the equivalent plots of figure 6(e–h) (e.g. compare the shape of the solid curve in figure 6e with that in 6h), it is far less than that caused by changes in thickness.

Overall, the predicted attenuation due to scattering in the MIZ is substantial, but this statement has to be taken in the context of the Pierson–Moskowitz spectrum

used, which is biased towards short to medium period waves. The manner in which wave energy decays as it proceeds through pack ice is dependent on its period, so if longer waves were present they would be far less affected by the ice floes encountered. On the other hand, the intensity of wind seas will quickly be reduced to insignificance.

Figure 7 is similar to figure 6, but in this case the ice floe separations, widths and thicknesses are chosen randomly. The results show the scattering for a single realization of common statistical distributions for these properties. Floe separations are selected from a uniform distribution defined between 10 m and 50 m, and floe widths are sampled from an exponential distribution $A \exp(-(x - x_{min})/\lambda)$ with $x_{min} = 10$ m and $\lambda = 40$ m, so the mean width is 50 m and 99% of the floes are less than 194 m across. The thicknesses are chosen from a beta distribution $Ax^{p-1}(1-x)^{q-1}$ with $p = q = 4$, $x \in [0, 1]$, mapped so that it has the mean stated in the figure, i.e. 0.5 m, 1 m, 1.5 m and 2.0 m and 20% maximum variation about that mean. The respective number of floes N in each case is the same as in figure 6. The plots display the same overall behaviour, e.g. the same dependence on thickness is evident, but the fine structure that arose from coherency in figure 6 has been replaced by incoherent fine structure that encapsulates the random distribution of floe thicknesses, diameters and spacings chosen – at least for the relatively small number of ice floes considered. In particular, the maxima and minima observed in the corresponding plots in figure 6 have decreased and increased, respectively. Williams & Squire (2004a) showed for a field of pressure ridges that this fine structure is smoothed out if results for different realizations of the various distributions of properties are averaged. They also showed that this average is approximated well by a ‘serial approximation’ and we would expect to see this here too if we introduced some averaging. The serial approximation turns out to be equivalent to the predictions of localization theory (Anderson 1958).

The fine structure is greatest in figure 7(h), i.e. for the largest number of floes ($N = 100$). While the smoothing effect of including very large numbers of floes from a prescribed distribution will diminish variability in relation to the incident Pierson–Moskowitz spectrum at any one period, the onset of this effect in terms of N will depend on the period under consideration and the characteristics of the floes present. It is evident that the reflection coefficients for individual ice floes combine to create a very complicated pattern for the marginal ice zone as a whole and that this causes the rather intricate metamorphosis of the incoming Pierson–Moskowitz spectrum on the far side of the modelled MIZ.

In figure 8, spectra arising from a Pierson–Moskowitz spectrum are plotted for MIZs randomized in the same way as figure 7, but for a single mean thickness of 1 m and values of $N = 500, \dots, 5000$ in steps of 500. Only periods between 8 s and 14 s are plotted because scattering has reduced the energy density to negligible proportions at lower periods and at longer periods the Pierson–Moskowitz spectrum has insignificant magnitude in any case. The substantial progressive selective filtering effect of the ice floes on the passage of the spectrum through the ice field is clear; as more and more floes are included, i.e. as we move from figures 8(a) to 8(j), the spectrum gradually progresses to the right towards longer periods. For 500 floes (figure 8a) the spectrum still has much absolute fine structure, with a substantial peak evident at a little above 9 s, but this is gradually reduced as more and more ice floes are incorporated into the simulation. Even for very large numbers of floes (figure 8j), notice that minimal divergence is evident above 12 s between the spectral shapes of the incident Pierson–Moskowitz spectrum (dotted) and the attenuated spectrum. This illustrates again the considerable dependence of the process on period and, in particular, that scattering impedes the passage of short periods while allowing long

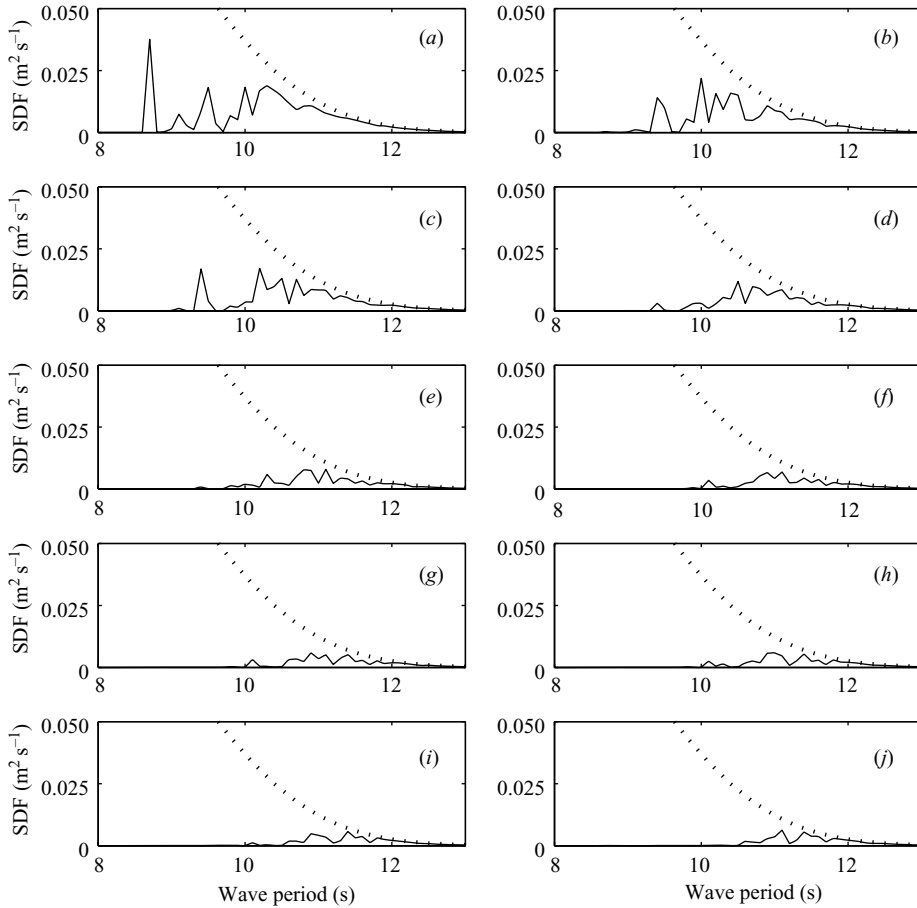


FIGURE 8. The scattering by N ice floes of random thickness, random width and random separation in a MIZ, located between a semi-infinite region of open water and a semi-infinite region of ice that has thickness 1 m. (Results apply to a single realization of the statistical distributions for these properties.) The graphs show the transmitted spectra arising from an incident Pierson–Moskowitz spectrum (shown dotted) for an MIZ composed of (a) $N = 500$, (b) 1000, (c) 1500, (d) 2000, (e) 2500, (f) 3000, (g) 3500, (h) 4000, (i) 4500 and (j) 5000 ice floes. The floes are drawn from a beta distribution with a 20% variation about a mean thickness of 1 m.

waves to pass unhindered, i.e. the system acts to low-pass filter the incoming wave energy in the manner observed in field observations (see, e.g. Squire & Moore 1980; Wadhams *et al.* 1986, 1987).

6. Conclusions

The theoretical development reported in this paper relates to wave propagation across three floating elastic thin plates – each with properties that can be defined independently, which are either welded together or have free edges. It also allows any of the plates to have zero thickness, i.e. to be absent, so that in those regions, the waves propagate on the free surface of open water. While this problem is straightforward

to define and is physically very relevant, it is mathematically difficult to solve. It has applicability to geophysics, in particular to wave propagation in ice-infested seas, and to marine engineering where the response of VLFSSs, floating breakwaters or compliant vessels in a seaway can be described.

The solution proceeds using the Wiener–Hopf method and residue calculus. It is validated in less complicated (less general) cases using published work that invokes different and independent methods of solution, so we have confidence that the analysis is accurate. A wide-spacing approximation that neglects the evanescent waves generated at each interface is included.

The theoretical model can be used to reproduce the way in which waves interact with various irregularities in continuous sea-ice, e.g. leads, icebergs, changes of material property and pressure ridges. It can also be extended to study wave propagation across large expanses of the Arctic sea-ice canopy, although this is not specifically discussed herein. Instead, the geophysical applications chosen to illustrate the work are wave propagation in (a) a deterministically-prescribed MIZ, where coherency-generated interference effects predominate; and (b) an ice field comprising floes selected from probability density functions that characterize the floe thickness, width and spacing, where incoherency occurs. Predictions are at least qualitatively consistent with field observations, noting that the physical morphology of the pack ice in the field data is not reported sufficiently precisely and in enough detail by Squire & Moore (1980) and Wadhams *et al.* (1986, 1987), for example, to allow a direct comparison of theory and data to be carried out. If this is to be conducted in the future, a more thorough survey of ice thickness alongside aerial photography (or active-radar-based remote sensing) to obtain floes size and spacing distributions, would be required.

This work was supported by a Marsden grant from the Royal Society of New Zealand and the University of Otago who provided a bridging grant to T.D.W.

Appendix. Proof that the potential in a region of constant properties may always be represented by an eigenfunction expansion

In this Appendix, we seek to justify the assumption that the potential ϕ may be represented by the expansion (4.1), without reference to the Wiener–Hopf solution in (3). In fact, the proof is valid for any number of adjacent regions and so will apply to a problem such as the one solved by Kohout & Meylan (2006). Similar proofs are also presented by Williams (2006) and Manam *et al.* (2005).

To achieve this we first use Green’s theorem to show that such an expansion always exists in a bounded region of constant properties (water depth, ice rigidity and mass per unit surface area; the ice may also have no free edges), and then let the region become unbounded to show that an expansion always exists in a semi-infinite region.

One point to note is that in the following, no assumptions are made about ε being zero or otherwise; since the Green’s functions we will use and the roots of the dispersion relation for each region will be continuous in ε , the expressions for ϕ in each region will also be continuous. Consequently, a corollary of this Appendix is that in §3 we are justified in first obtaining $\phi(x, z)$ when $\varepsilon > 0$ and then taking the limit as $\varepsilon \rightarrow 0$.

A.1. Bounded regions

Let ϕ satisfy (2.2) in the region $\Omega_{\mathbb{N}} = \{(\xi, \zeta) \mid x_0 < \xi < x_1 \text{ and } 0 < \zeta < H\}$, where $\mathcal{L}(\partial_x) = \mathcal{L}_{\mathbb{N}}(\partial_x) = D_{\mathbb{N}}(\partial_x - \alpha^2)^2 + \lambda - m_{\mathbb{N}}\mu$ in (2.2c), and let $G_{\mathbb{N}}$ satisfy (3.1), but with

(3.1b) replaced by

$$\mathcal{L}_{\aleph}(\partial_{\xi})G_{\aleph,\zeta}(x - \xi, z, 0) + G_{\aleph}(x - \xi, z, 0) = 0. \quad (\text{A } 1)$$

From (3.2), G_{\aleph} can be written as

$$G_{\aleph}(x - \xi, z, 0) = i \sum_{\alpha \in S_{\aleph}} \hat{A}_{\aleph}(\alpha) e^{i\alpha|x-\xi|} \varphi(z, \alpha) \varphi(\zeta, \alpha), \quad (\text{A } 2)$$

where S_{\aleph} and $\hat{A}_{\aleph}(\alpha)$ are the \aleph th-region analogues of the S_j and $\hat{A}_j(\alpha)$ defined in § 3.1 for the j th region. Similarly, in the working below, α_{\aleph} and $\varphi_{\aleph}(z)$ are the \aleph th-region analogues of α_j and $\varphi_j(z)$.

Applying Green's theorem to ϕ directly (as opposed to applying it to ψ as we did in equation 3.4a), let us write

$$\begin{aligned} \phi(x, z) &= \oint_{\partial\Omega_{\aleph}} (\partial_n G_{\aleph} \phi - G_{\aleph} \partial_n \phi) ds \\ &= \int_0^H (G_{\aleph,x}(x - x_0, z, \zeta) \phi(x_0, \zeta) + G_{\aleph}(x - x_0, z, \zeta) \phi_x(x_0, \zeta)) d\zeta \\ &\quad - \int_0^H (G_{\aleph,x}(x - x_1, z, \zeta) \phi(x_1, \zeta) + G_{\aleph}(x - x_1, z, \zeta) \phi_x(x_1, \zeta)) d\zeta \\ &\quad - \int_{x_0}^{x_1} (G_{\aleph,\zeta}(x - \xi, z, 0) \phi(\xi, 0) - G_{\aleph}(x - \xi, z, 0) \phi_z(\xi, 0)) d\xi. \end{aligned} \quad (\text{A } 3)$$

By eliminating ϕ and G_{\aleph} from the final integral using (2.2b) and (A 1) (as we did in § 3.2) and integrating by parts, that integral simplifies to

$$(\mathbf{P}_{x_0}^+)^T \mathcal{L}_{\text{edge}(\partial_x)} G_{\aleph,\zeta}(x - \xi_0, z, 0) - (\mathbf{P}_{x_1}^-)^T \mathcal{L}_{\text{edge}(\partial_x)} G_{\aleph,\zeta}(x - \xi_1, z, 0),$$

so by substituting (A 2) into (A 3), we obtain the eigenfunction expansion

$$\phi(x, z) = \sum_{\alpha \in S_{\aleph}} (\hat{b}_{\aleph}(\alpha) \exp(i\alpha(x - x_0)) + \hat{c}_{\aleph}(\alpha) \exp(i\alpha(x_1 - x))) \varphi(z, \alpha), \quad (\text{A } 4)$$

where

$$\hat{b}_{\aleph}(\alpha) = i \hat{A}_{\aleph}(\alpha) \left(\mathbf{p}^T(-\alpha) \mathbf{P}_{x_0}^+ \varphi_z(0, \alpha) + \int_0^H (i\alpha \phi(x_0, \zeta) + \phi_x(x_0, \zeta)) d\zeta \right), \quad (\text{A } 5a)$$

$$\hat{c}_{\aleph}(\alpha) = i \hat{A}_{\aleph}(\alpha) \left(-\mathbf{p}^T(\alpha) \mathbf{P}_{x_1}^- \varphi_z(0, \alpha) + \int_0^H (i\alpha \phi(x_1, \zeta) - \phi_x(x_1, \zeta)) d\zeta \right). \quad (\text{A } 5b)$$

Thus, we have proved that if ϕ satisfies (2.2) in a bounded region where \mathcal{L} has continuous constant coefficients then it can always be expanded in terms of eigenfunctions; and in particular, if we set $x_0 = 0$, $x_1 = l$, $\hat{b} = \hat{b}_{\aleph}$ and $\hat{c} = \hat{c}_{\aleph}$ in (A 4), we have proved that we are able to write ϕ in the form it takes for $0 < x < l$ in (4.1).

A.2. Semi-infinite regions

We can generate an eigenfunction expansion for ϕ if the region Ω_{\aleph} is unbounded by letting either $x_0 \rightarrow -\infty$ or $x_1 \rightarrow \infty$ in (A 3) and substituting the known asymptotic behaviour of G_{\aleph} and the radiation conditions (3.3) for ϕ into the integral.

We will deal with the case as $\xi = x_0 \rightarrow -\infty$ first. If we do that then

$$G_{\aleph}(x - \xi, z, \zeta) \sim i \hat{A}_{\aleph}(\alpha_{\aleph}) \exp(i\alpha_{\aleph}|x - \xi|) \varphi_{\aleph}(z) \varphi_{\aleph}(\zeta), \quad (\text{A } 6a)$$

$$\phi(x, z) \sim (I \exp(i\alpha_{\aleph} \xi) + R \exp(-i\alpha_{\aleph} \xi)) \varphi_{\aleph}(z), \quad (\text{A } 6b)$$

and substituting (A 6a) into (A 3) implies that ϕ is now

$$\phi(x, z) = \lim_{x_0 \rightarrow \infty} b_N(\alpha_N) \exp(i\alpha_N(x - x_0))\varphi_N(z) + \sum_{\alpha \in S_N} \hat{c}_N(\alpha) \exp(i\alpha(x_1 - x))\varphi(z, \alpha). \quad (\text{A } 7)$$

Substituting (A 6b) into the definition of $b_N(\alpha_N)$ we may write it as

$$b_N(\alpha_N) = -2\alpha_N \hat{A}_N(\alpha_N) I \exp(i\alpha_N x_0) \left(2D_N \gamma^2(\alpha_N) (\varphi'_N(0))^2 + \int_0^H \varphi_N^2(\zeta) d\zeta \right), \quad (\text{A } 8)$$

which evaluates to $I \exp(i\alpha_N x_0)$ when we use the integral rule (4.5). Thus, ϕ is simply

$$\phi(x, z) = I \exp(i\alpha_N(x - x_0))\varphi_N(z) + \sum_{\alpha \in S_N} \hat{c}_N(\alpha) \exp(i\alpha(x_1 - x))\varphi(z, \alpha). \quad (\text{A } 9)$$

Setting $I = 1$, $x_1 = 0$, and $\hat{a}(\alpha) = \hat{c}_N(\alpha)$ allows us to write ϕ in its $x < 0$ form in (4.1).

Similarly, if we let $x_1 \rightarrow \infty$ in (A 4) and this time substitute (A 6) into the terms that are evaluated at $\xi = x_1$ (but replacing I with T and R with 0 in equation (A 6b)), we find that ϕ can be written

$$\phi(x, z) = \sum_{\alpha \in S_N} \hat{b}_N(\alpha) \exp(i\alpha(x - x_0))\varphi(z, \alpha). \quad (\text{A } 10)$$

Setting $x_0 = l$ and $\hat{d}(\alpha) = \hat{b}_N(\alpha)$ means we have derived the $x > l$ form for ϕ in (4.1).

REFERENCES

- ANDERSON, P. W. 1958 Absence of diffusion in certain random lattices. *Phys. Rev.* **109**, 1492–1505.
- BALMFORTH, N. J. & CRASTER, R. V. 1999 Ocean waves and ice sheets. *J. Fluid Mech.* **395**, 89–124.
- BARRETT, M. & SQUIRE, V. A. 1996 Ice-coupled wave propagation across an abrupt change in ice rigidity, density or thickness. *J. Geophys. Res.* **101** (C9), 20825–20832.
- CHAKRABARTI, A. 2000 On the solution of the problem of scattering of surface-water waves by the edge of an ice cover. *Proc. R. Soc. Lond.* **A 456**, 1087–1099.
- CHOU, T. 1998 Band structure of surface flexural-gravity waves along periodic interfaces. *J. Fluid Mech.* **369**, 333–350.
- CHUNG, H. & FOX, C. 2002a Calculation of wave-ice interaction using the Wiener-Hopf technique. *NZ J. Maths* **31**, 1–18.
- CHUNG, H. & FOX, C. 2002b Propagation of flexural-gravity waves at the interface between floating plates. *Intl J. Offshore Polar Engng* **12** (3), 163–170.
- CHUNG, H. & LINTON, C. M. 2005 Reflection and transmission of waves across a gap between two semi-infinite elastic plates on water. *Q. J. Mech. Appl. Maths* **58** 1–15.
- COMISO, J. 2002 A rapidly declining perennial sea-ice cover in the Arctic. *Geophys. Res. Lett.* **29** (20), 1956, doi:10.1029/2002GL015650.
- EVANS, D. V. & DAVIES, T. V. 1968 Wave-ice interaction. *Tech. Rep.* 1313. Davidson Laboratory, Stevens Institute of Technology, New Jersey.
- EVANS, D. V. & PORTER, R. 2003 Wave scattering by narrow cracks in ice sheets floating on water of finite depth. *J. Fluid Mech.* **484**, 143–165.
- FOX, C. & SQUIRE, V. A. 1990 Reflection and transmission characteristics at the edge of shore fast sea ice. *J. Geophys. Res.* **95**, 11 629–11 639.
- FOX, C. & SQUIRE, V. A. 1994 On the oblique reflexion and transmission of ocean waves from shore fast sea ice. *Phil. Trans. R. Soc. Lond.* **A 347** (1682), 185–218.
- GOL'DSHTEIN, R. V. & MARCHENKO, A. V. 1989 Diffraction of plane gravitational waves by the edge of an ice cover. *J. Appl. Math. Mech.* **53**, 731–736.
- HERMANS, A. J. 2003 Interaction of free surface waves with a floating dock. *J. Engng Maths* **45**, 39–53.
- KOHOUT, A. L. & MEYLAN, M. H. 2006 A model for wave scattering in the marginal ice zone based on a two-dimensional floating elastic plate solution. *Ann. Glaciol.* In press.

- LAWRIE, J. B. & ABRAHAMS, I. D. 1999 An orthogonality relation for a class of problems with high-order boundary conditions; applications in sound–structure interaction. *Q. J. Mech. Appl. Maths* **52**, 161–181.
- LINTON, C. & CHUNG, H. 2004 Reflection and transmission at the ocean/sea-ice boundary. *Wave Motion* **33**, 43–52.
- LINTON, C. M. & MCIVER, P. 2001 *Handbook of Mathematical Techniques for Wave/Structure Interactions*. CRC Press.
- MANAM, S. R., BHATTACHARJEE, J. & SAHOO, T. 2005 Expansion formulae in wave structure interaction problems. *Proc. R. Soc. Lond. A* **462**, 263–287.
- MARCHENKO, A. V. 1997 Flexural gravity wave diffraction at linear irregularities in sheet ice. *Fluid Dyn.* **32**, 548–560.
- MEYLAN, M. H. 1993 The behaviour of sea ice in ocean waves. PhD thesis, University of Otago.
- MEYLAN, M. H. & MASSON, D. 2006 A linear Boltzmann equation to model wave scattering in the marginal ice zone. *Ocean Modelling* **11**, 417–427.
- MEYLAN, M. H. & SQUIRE, V. A. 1994 The response of ice floes to ocean waves. *J. Geophys. Res.* **99**, 899–900.
- MEYLAN, M. H. & SQUIRE, V. A. 1996 Response of a circular ice floe to ocean waves. *J. Geophys. Res.* **101** (C4), 8869–8884.
- MEYLAN, M. H., SQUIRE, V. A. & FOX, C. 1997 Toward realism in modelling ocean wave behaviour in marginal ice zones. *J. Geophys. Res.* **102** (C10), 22981–22991.
- NOBLE, B. 1958 *Methods Based on the Wiener–Hopf Technique for the Solution of Partial Differential Equations*. Pergamon.
- PETER, M. A., MEYLAN, M. H. & LINTON, C. M. 2006 Water-wave scattering by a periodic array of arbitrary bodies. *J. Fluid Mech.* **548**, 237–256.
- PIERSON, W. J. & MOSKOWITZ, L. 1964 A proposed spectral form for fully developed wind seas based on the similarity theory of S. A. Kitaigorodskii. *J. Geophys. Res.* **69**, 5181–5190.
- PORTER, D. & PORTER, R. 2004 Approximations to wave scattering by an ice sheet of variable thickness over undulating bed topography. *J. Fluid Mech.* **509**, 145–179.
- ROOS, B. W. 1969 *Analytical Functions and Distributions in Physics and Engineering*. Wiley.
- ROTHROCK, D. A., YU, Y. & MAYKUT, G. A. 1999 Thinning of the Arctic sea-ice cover. *Geophys. Res. Lett.* **26**, 3469–3472.
- SAHOO, T., YIP, T. L. & CHWANG, A. T. 2001 Scattering of surface waves by a semi-infinite floating elastic plate. *Phys. Fluids* **13**, 3215–3222.
- SQUIRE, V. A. & DIXON, T. W. 2000 An analytic model for wave propagation across a crack in an ice sheet. *Intl J. Offshore Polar Engng* **10** (3), 173–176.
- SQUIRE, V. A. & DIXON, T. W. 2001a How a region of cracked sea ice affects ice-coupled wave propagation. *Ann. Glaciol.* **33**, 327–332.
- SQUIRE, V. A. & DIXON, T. W. 2001b On modelling an iceberg embedded in shore fast sea ice. *J. Engng Maths* **40** (3), 211–236.
- SQUIRE, V. A., DUGAN, J. P., WADHAMS, P., ROTTIER, P. J. & LIU, A. K. 1995 Of ocean waves and sea ice. *Annu. Rev. Fluid Mech.* **27**, 115–168.
- SQUIRE, V. A. & MOORE, S. C. 1980 Direct measurement of the attenuation of ocean waves by pack ice. *Nature* **283**, 365–368.
- TKACHEVA, L. A. 2001 Scattering of surface waves by the edge of a floating elastic plate. *J. Appl. Mech. Tech. Phys.* **42**, 638–646.
- TKACHEVA, L. A. 2002 Diffraction of surface waves at a thin elastic floating plate. In *Proc. 17th International Workshop on Water Waves and Floating Bodies, Cambridge, UK*, pp. 104–107.
- TKACHEVA, L. A. 2004 The diffraction of surface waves by a floating elastic plate at oblique incidence. *Z. Angew. Math. Mech.* **68**, 425–436.
- WADHAMS, P. & DAVIS, N. R. 2000 Further evidence of ice thinning in the Arctic ocean. *Geophys. Res. Lett.* **27** (24), 3973–3976.
- WADHAMS, P., SQUIRE, V. A., EWING, J. A. & PASCAL, R. W. 1986 The effect of the marginal ice zone on the directional wave spectrum of the ocean. *J. Phys. Oceanogr.* **16**, 358–376.
- WADHAMS, P., SQUIRE, V. A., GOODMAN, D. J., COWAN, A. M. & MOORE, S. C. 1987 The attenuation of ocean waves in the marginal ice zone. *J. Geophys. Res.* **93** (C6), 6799–6818.
- WILLIAMS, T. D. 2006 Reflections on ice: the scattering of flexural–gravity waves by irregularities in arctic and antarctic ice sheets. PhD thesis, University of Otago.

- WILLIAMS, T. D. & SQUIRE, V. A. 2002 Wave propagation across an oblique crack in an ice sheet. *Intl J. Offshore Polar Engng* **12** (3), 157–162.
- WILLIAMS, T. D. & SQUIRE, V. A. 2004a Oblique scattering of plane flexural–gravity waves by heterogeneities in sea ice. *Proc. R. Soc. Lond. A* **460**, 3469–3497.
- WILLIAMS, T. D. & SQUIRE, V. A. 2004b The scattering of flexural–gravity waves by an ice field. *Int. J. Offshore Polar Engng* **14** (3), 161–168.
- WILLIAMS, T. D. & SQUIRE, V. A. 2006 Wave scattering at the sea-ice/ice-shelf transition with other applications. *SIAM J. Appl. Maths.* Submitted.